Astronomy & Astrophysics manuscript no. output
November 12, 2026
©ESO 2026

Euclid Data Release 1 (DR1)

Euclid photometric masks

Euclid Collaboration: J. Odier, J. F. Macias-Perez, G. Alguero, C. Benoist, M. Radovich, P. Corcho-Caballero, H. Aussel, P. Casenove, et al.

(Full author list and affiliations details can be found after the references)

November 12, 2026

ABSTRACT

This paper describes the Euclid DR1 photometric masks, which trace spatial variations in the survey properties (e.g. satellite position angles, integration time, sky tiling, and survey footprint); in the instrumental performance of *Euclid* and the external data (EXT) it uses (e.g. survey coverage, depth, PSF width, quality flags, systematic effects and astrometric uncertainties); and in possible contamination from sky emission (e.g. galactic extinction and zodiacal light emission). Among this, the effective coverage mask is particularly important as it defines the effective survey area and can be used to exclude spurious objects when selecting *Euclid* photometric samples for scientific analyses. The *Euclid* photometric masks are built for each observed sky region (tile) and are provided as full-sky `HEALPix` maps (nested ordering and explicit indexing) at $N_{\rm side} = 16\,384$, equating to a resolution of $12\farcs88$, for both the Euclid Wide Survey (EWS) and Euclid Deep Survey (EDS). We estimate the total area of the DR1 EWS (EDS) to be 2008.8 (74.7) deg^2 and find that 82 (81)% of this area is preserved by the effective coverage mask. We observe that *Euclid*'s instrumental properties are consistent with expectations, showing only minor relative variations across the sky. For DR1 EWS the standard deviation of the depth (computed for a $2''$ aperture and at 5 σ) is below 0.2 AB mag, with median values of 25.69, 24.14, 24.3, and 24.29 for the *Euclid* $I_{\rm E}$, $Y_{\rm E}$, $J_{\rm E}$, and $H_{\rm E}$ bands. Finally, we expect these photometric masks to be key to many science applications and in particular for cosmological analyses.

Key words. Methods: observational – Surveys – Galaxies: photometry – Cosmology: observations

1. Introduction

The *Euclid* satellite mission (Euclid Collaboration: Mellier et al. 2025), launched in July 2023, aims to constrain the main cosmological parameters through two primary cosmological probes: gravitational lensing and galaxy clustering (Amendola et al. 2018; Euclid Collaboration: Blanchard et al. 2020). To this end, it will collect data over the 14 000 deg^2 Euclid Wide Survey (EWS) and the approximately 63 deg^2 Euclid Deep Survey (EDS; Euclid Collaboration: Scaramella et al. 2022)[1].

Euclid has two instruments (Euclid Collaboration: Scaramella et al. 2022): the Visible instrument (VIS, Euclid Collaboration: Cropper et al. 2025) and the Near Infrared Spectrometer and Photometer (NISP, Euclid Collaboration: Jahnke et al. 2025). VIS was designed to provide exquisite imaging in the optical domain for galaxy detection and shear measurements. It consists of a single visible band, $I_{\rm E}$. NISP provides photometric imaging in three bands, $Y_{\rm E}$, $J_{\rm E}$, and $H_{\rm E}$, for detecting distant galaxies, as well as spectroscopic redshifts for galaxy clustering. The *Euclid* data are combined with external data (referred to as 'EXT', see Euclid Collaboration: Corcho-Caballero et al. 2026, for more details) from ground-based photometric surveys such as the Dark Energy Survey (DES, Abbott et al. 2021), the Canada-France Imaging Survey (CFIS, Ibata et al. 2017), the Panoramic Survey Telescope and Rapid Response System on Maui (Pan-STARRS, Magnier et al. 2020), The Waterloo-Hawaii-IfA G-band Survey (WHIGS), and the Wide Imaging with Subaru HSC of the Euclid Sky (WHISHES, Aihara et al. 2018) to determine photometric redshifts for all VIS- and NISP-detected objects (Euclid Collaboration: Hartley et al. 2026).

The processing of *Euclid* data (see Euclid Collaboration: Ruffenach et al. 2026, for a detailed description) is organised within the *Euclid* Science Ground Segment (SGS) into pipelines and processing functions (PFs). Each PF is developed and maintained by a corresponding Organisational Unit (OU) within the SGS. This paper describes the OU-LE3 (Organizational Unit Level 3) VMPZ-ID (Visibility Mask PhotoZ-Internal Data) PF (Processing Function) and associated pipelines contributing to the core products of Euclid Data Release 1 (DR1 Euclid Data Release 1 2026), also known as DR1 Foundation. An overview of the DR1 Foundation products is given in Euclid Collaboration: Aussel et al. (2026b). The DR1 sky survey (Euclid Collaboration: Tereno et al. 2026) comprises about 2000 deg^2 of the EWS and the three EDS subfields: Euclid Deep Field Fornax (EDF-F), South (EDF-S), and North (EDF-N). Some Euclid Auxiliary Fields and calibration fields are also released.

The main VMPZ-ID products are `HEALPix`[2] (Górski et al. 2005) sky maps, which are called photometric masks hereafter, tracking spatial variations in the properties of the *Euclid* survey, the instrumental performance of VIS and NISP, the quality of EXT data, and foreground sky emission. These variations could propagate into the final *Euclid* catalogues and bias the estimation of cosmological parameters, as reported for other photometric surveys, such as KiDS and DES (see Weaverdyck et al.

[1] https://www.cosmos.esa.int/web/euclid/euclid-survey

[2] Hierarchical Equal Area isoLatitude Pixelation of a sphere, see https://healpix.sourceforge.io/

2026; Yan et al. 2025, and references therein). These masks will be also useful in selecting *Euclid* galaxy samples for statistical studies in non-cosmological analyses.

The main inputs to the VMPZ-ID PF are merged sky images and associated RMS noise and flags (see Euclid Collaboration: Kümmel et al. 2026, for further description). Star catalogues and star polygons including the central diffraction lobe and diffraction spikes, which are constructed from the *Gaia* survey, are also used (Gaia Collaboration et al. 2016).

This document is structured as follows. Section 2 presents the VMPZ-ID pipeline and the products delivered in DR1. Section 3 details the VMPZ-ID photometric masks, Sect. 4 discusses the main EWS photometric masks, and Sect. 5 describes the masks for the EDFs. Conclusions are presented in Sect. 6.

2. VMPZ-ID pipeline and products

The DR1 VMPZ-ID pipeline is based on the Q1 pipeline described in Euclid Collaboration: Aussel et al. (2026a) and has since been improved and extended to include additional sky masks. Information associated to the VIS, NIR, and EXT MER (MERge processing, Euclid Collaboration: Kümmel et al. 2026) images at exposure (e.g. integration time, star polygons, satellite position angles, PSF width) and tile (e.g. image footprint, mask flags and noise) levels is combined into a series of masks in the `HEALPix` format using nested ordering, explicit indexing and $N_{\rm side} = 16\,384$, which corresponds to a resolution of approximately $12\farcs88$. This resolution was selected as a good compromise between usability, allowing for loading an all-sky mask in the memory of a *Euclid* Science Data Centre node, and preserving as much as possible of the fine spatial information given by the pixel scale masks of the original MER images (Euclid Collaboration: Kümmel et al. 2026). VMPZ-ID also produces, at the same resolution, the so-called `DpdHealpixInfoMapVMPZ` product, which enables satellite and instrumental properties to be tracked and projected onto the sky. This allows straightforward cross-checks between spatial information (for example, the noise at a given point in the survey) and temporal information (for example, the value of a temperature sensor on the *Euclid* focal plane), and facilitates searches for possible effects on *Euclid* performance. Finally, random galaxy catalogues are also produced to mimic spatial variations in the combined coverage of all bands used for photometry.

2.1. Pipeline

VMPZ-ID is the first OU-LE3 PF to be executed after OU-LE2 processing (Euclid Collaboration: Ruffenach et al. 2026). The photometric masks are constructed from MER data products and *Gaia* cutouts (Euclid Collaboration: Kümmel et al. 2026) at the tile (see tessellation scheme in Euclid Collaboration: Scaramella et al. 2022) level using two main pipelines named `VMPZ_Star_Pipeline` and `VMPZ_Mosaic_Pipeline`. These two pipelines are triggered by the operations team, as described in Euclid Collaboration: Ruffenach et al. (2026), as soon as the MER (see Euclid Collaboration: Kümmel et al. 2026, for details) data products are available for a given tile. The `VMPZ_Star_Pipeline` mainly produces masks related to properties of the stellar distribution on the sky. The `VMPZ_Mosaic_Pipeline` handles survey, satellite, instrumental and sky properties.

2.2. Main data products

The main products of the `VMPZ_Star_Pipeline` and `VMPZ_Mosaic_Pipeline` pipelines consist of the following six main types of photometric masks and a random catalogue.

- `DpdHealpixFootprintMaskVMPZ`: integer values, equal to 1 if the sky region has been observed and 0 otherwise.
  For DR1, instances have been produced for the *Euclid* bands, $I_{\rm E}$, $J_{\rm E}$, $H_{\rm E}$, and $Y_{\rm E}$, and for all available external bands (Euclid Collaboration: Corcho-Caballero et al. 2026).

- `DpdHealpixCoverageVMPZ`: float values between 0 and 1, representing the coverage, i.e., the fraction of `HEALPix` pixels covered by the available valid data for each of the *Euclid* and EXT bands, as for `DpdHealpixFootprintMaskVMPZ`.

- `DpdHealpixEffectiveCoverageVMPZ`: float values between 0 and 1, representing the effective coverage, i.e., the fraction of `HEALPix` pixels covered by valid data combining the *Euclid* and EXT bands.

- `DpdHealpixBitMaskVMPZ`: unsigned integer values whose bits are associated with the flags of the `MerBksMosaic` (see Euclid Collaboration: Kümmel et al. 2026, for details).

- `DpdHealpixDepthMapVMPZ`: float values representing the RMS-derived depth for each *Euclid* and EXT band.

- `DpdHealpixInfoMapVMPZ`: float values representing different quantities of interest. To discriminate between the masks associated to different physical quantities we define the so-called `InfoMap` type as described in Sect. 3 and Table.1.

- `DpdHealpixRandomCatalogueVMPZ`: generic container for storing simulated galaxy catalogues.

3. Detailed mask description

The VMPZ-ID pipelines have produced 104 photometric masks for DR1. Table 1 summarises the main properties of these masks. A more detailed description of each mask is given below. We warn the reader that these masks present in some cases redundant or correlated information.

3.1. Survey-definition masks and random catalogues

The main masks accounting for the *Euclid* survey coverage and the spatial distribution of the EXT data are presented here.

- Tile index: for each `HEALPix` pixel, it encodes the number of the MER tile on which it lies. This is stored as a `DpdHealpixInfoMapVMPZ` product with information map type `Tile`. Tile numbers are given as signed 64-bit integers.

- Footprint: defines the observed or valid sky area. This is stored as a `DpdHealpixFootprintMaskVMPZ` product with a weight of 1 for valid `HEALPix` pixels. It is available for the *Euclid* and EXT bands. The mask is constructed from the `MerBksMosaic` maps, with observed sky regions set to 1 and the others to 0. Additional flagging at the MER processing level, encoded in the `MerBksMosaic` RMS maps, is also taken into account. MER tile pixels with zero RMS or above a given fixed threshold, $\sigma_{\rm thresh} = 10\,000$ ADU, are considered unobserved and treated accordingly when

Table 1. Summary of the main characteristics of the photometric masks produced by VMPZ-ID.

Mask name	Mask family	Mask product type	Information map type	Numerical type	Units	Per-band mask
Tile index	Survey	`DpdHealpixInfoMapVMPZ`	Tile	int64	...	no
Solar aspect angle	Survey/Satellite	`DpdHealpixInfoMapVMPZ`	SAA	float32	deg	no
Alpha angle	Survey/Satellite	`DpdHealpixInfoMapVMPZ`	AA	float32	deg	no
Beta angle	Survey/Satellite	`DpdHealpixInfoMapVMPZ`	BA	float32	deg	no
Integration time	Survey	`DpdHealpixInfoMapVMPZ`	Exposures	float32	sec	*Euclid* only
Footprint	Survey/Instrument	`DpdHealpixFootprintMaskVMPZ`	...	float32	...	yes
Coverage	Survey/Instrument	`DpdHealpixCoverageMaskVMPZ`	...	float32	...	yes
Effective coverage	Survey/Instrument	`DpdHealpixEffectiveCoverageMaskVMPZ`	...	float32	...	combined
Bit mask	Instrument	`DpdHealpixBitMaskVMPZ`	...	uint32	...	yes
Depth	Instrument	`DpdHealpixDepthMapVMPZ`	...	float32	AB mag	yes
RMS noise	Instrument	`DpdHealpixInfoMapVMPZ`	Noise	float32	ADU	yes
Point-spread function	Instrument	`DpdHealpixInfoMapVMPZ`	PSF	float32	arcsec	yes
Persistence	Instrument	`DpdHealpixInfoMapVMPZ`	Persistence	float32	...	NIR only
NIR PRMS	Instrument	`DpdHealpixInfoMapVMPZ`	NIR_PRMS	float32	mas	NIR only
Pan-STARRS artefacts	Instrument	`DpdHealpixInfoMapVMPZ`	PanStarrsArtefacts	float32	...	Pan-STARRS only
Zodiacal light	Sky/Instrument	`DpdHealpixInfoMapVMPZ`	ZodiacalLight	float32	erg cm^{-2} Å^{-1} arcsec^{-2}	*Euclid* only
Galactic extinction	Sky/Instrument	`DpdHealpixInfoMapVMPZ`	GalacticExtinction	float32	mag	*Euclid* only
Star number density	Sky emission	`DpdHealpixInfoMapVMPZ`	StarNumberDensity	float32	counts/pixel	no
Star mean flux	Sky emission	`DpdHealpixInfoMapVMPZ`	StarBrightnessMean	float32	e$^-$/s	*Gaia G*
Star RMS flux	Sky emission	`DpdHealpixInfoMapVMPZ`	StarBrightnessRms	float32	e$^-$/s	*Gaia G*
Star std flux	Sky emission	`DpdHealpixInfoMapVMPZ`	StarBrightnessStd	float32	e$^-$/s	*Gaia G*

Notes. For each mask, the table gives the mask family (indicating whether it is related to survey properties, satellite status, instrument performance, or sky emission), the information map type as defined in the text, information map type (only for the `DpdHealpixInfoMapVMPZ` masks) and the numerical type. It also indicates whether the masks are produced per band, including *Euclid* and EXT bands. *Gaia G* band is defined in https://www.cosmos.esa.int/web/gaia/edr3-passbands/

computing the footprint. Finally, all MER tile pixels lying within a `HEALPix` pixel are combined using a logical `OR` operator.

– Coverage: determines the relative coverage, float number between 0 and 1, for each `HealPix` pixel and for each *Euclid* and EXT band. The coverage per band (*Euclid* and EXT) is calculated from the `MerBksMosaic` maps. MER tile pixels for which the RMS value is zero or exceeds $\sigma_{\rm thresh}$ are considered unobserved. Furthermore, for the *Euclid* bands, polygonal masks are used to exclude sky regions affected by bright-star emission. For each `HEALPix` pixel, the coverage is given by the fraction of valid MER tile pixels.

– Effective coverage: defines the fraction of sky simultaneously observed in all photometric bands. An initial effective coverage mask is constructed at the MER mosaic resolution ($19\,200 \times 19\,200$ pixels), before projection onto the `HEALPix` grid. As defined the initial effective coverage mask is binary (either 0 or 1) while the `HEALPix` one can have float values between 0 and 1. In this initial mask, for each available VIS, NIR, or EXT band, MER tile pixels for which the RMS value is zero or above $\sigma_{\rm thresh}$ are considered unobserved. In some cases, multiple EXT data sets in equivalent photometric bands (e.g. HSC *R*, HSC *R*2, HSC *I*, HSC *I*2) are used to cover the same tile. To handle this, effective EXT bands are defined; for each of them, multiple input data sets are available, and their validity masks are first combined using a logical `OR` operator. The masks from the different effective bands are then combined using a logical `AND` operator, thereby retaining only regions observed in all effective bands.

Regions affected by bright stars are subsequently excluded. For the $I_{\rm E}$, $Y_{\rm E}$, $J_{\rm E}$, and $H_{\rm E}$ bands, when stellar polygons describing stellar lobes and diffraction spikes are available, they are directly rasterised onto the initial MER effective coverage grid. For the EXT data, an additional mask is constructed using *Gaia* star catalogues. Stars with magnitude in the *G* red band $G_{\rm RP} < 14$ are masked[3] with circular regions whose radii, expressed in arcmin, follow the empirical relation (see left panel of Fig. 1)

$$r_*(G_{\rm RP}) = -0.01972\,G_{\rm RP}^3 + 0.65849\,G_{\rm RP}^2 - 7.31734\,G_{\rm RP} + 27.75053. \quad (1)$$

The resulting radii are enlarged by 20% when constructing the circular masks to minimise the number of spurious detections while preserving galaxy counts in the final *Euclid* catalogues. Bleeding trails (see Desai et al. 2016, for a discussion) are additionally masked for stars with $G_{\rm RP} < 10.3$; their width is described by the empirical polynomial (see Fig. 1 b)

$$r_{\rm bleed}(G_{\rm RP}) = +0.06158\,G_{\rm RP}^4 - 1.98886\,G_{\rm RP}^3 + 23.65131\,G_{\rm RP}^2 - 123.78714\,G_{\rm RP} + 245.65947, \quad (2)$$

with the polynomial value saturated at $G_{\rm RP} = 4$ for the brightest stars. The resulting rectangular masks have a magnitude-dependent total angular width of $2\,r_{\rm bleed}$ and a

[3] The *Gaia G* red band magnitude, $G_{\rm RP}$, is defined in https://www.cosmos.esa.int/web/gaia/edr3-passbands/

fixed extent of 0.″488 in the perpendicular direction to the bleed.

A pre-selected set of extended objects is also masked. This set comprises globular clusters and planetary nebulae from the New General Catalogue[4] (NGC) and nearby galaxies from the Siena Galaxy Atlas[5] (SGA). NGC objects are masked using their radii, while SGA galaxies with an approximate Vega magnitude of `MAG_LEDA` < 16.5 are masked using elliptical regions Bleeding on their major and minor axes and position angles, with their dimensions enlarged by 30%. The resulting initial effective coverage mask is projected and averaged onto an $N_{\rm side} = 16\,384$ `HEALPix` grid to produce the final effective coverage mask. This mask is saved as a `DpdHealpixEffectiveCoverageMaskVMPZ` product.

Additionally, the initial effective coverage mask is used to construct a flag called `EFF_COV` for each object in the `DpdMerFinalCatalog`. This flag is 1 if the object position[6] lies on a pixel with non-zero initial effective coverage, and 0 otherwise. This flag is stored in the second extension of the effective coverage FITS[7] file.

- Random catalogues: random galaxy catalogues are generated from a uniform distribution weighted at each position by the effective coverage value. The positions of the simulated galaxies (RA and Dec) are stored as tables in `DpdHealpixRandomCatalogueVMPZ` products for each tile. Figure 2 shows an example of a random catalogue.

3.2. Survey-related masks

Masks related to the satellite's position and integration time during operations are presented here.

- Solar aspect angle: defines the *Euclid* satellite solar aspect angle in degrees as described in Euclid Collaboration: Scaramella et al. (2022). This is stored in a `DpdHealpixInfoMapVMPZ` information map of type `SAA`. It is computed from the MER layering files, which contain both the integration time and the satellite angles for each exposure. The final mask is obtained by computing the exposure-time-weighted mean value for each `HEALPix` pixel.

- Alpha/beta angles: defines the *Euclid* satellite Alpha and Beta angles in degrees (Euclid Collaboration: Scaramella et al. 2022). Both are computed and stored like `SAA`, using information map types `AA` and `BA`, respectively.

- Exposures: for each of the *Euclid* bands, this represents the total integration time in seconds per `HEALPix` pixel and is calculated from the MER layering files described above. This is stored as a `DpdHealpixInfoMapVMPZ` product.

[4] Bleeding trails on the OpenNGC (NGC/IC objects) catalogue. See https://www.legacysurvey.org/dr9/external/ and https://github.com/mattiaverga/OpenNGC/ .

[5] Based on the 2020 version of the Siena Galaxy Atlas, SGA-2020. See https://www.legacysurvey.org/dr9/external/ and https://www.legacysurvey.org/sga/sga2020/ .

[6] Notice that we do not take into account the object extension

[7] Flexible Image Transport System: https://heasarc.gsfc.nasa.gov/docs/heasarc/fits.html

3.3. Instrumental-property masks

For each of the *Euclid* and EXT bands, masks of the main instrumental properties are obtained from the `MerBksMosaic` maps. For each `HEALPix` pixel, the weighted average of the instrumental properties is computed. As for the previously described masks, zero weight is assigned to MER tile pixels with RMS equal to zero or above a given threshold representing bad or corrupted data.

- RMS noise: represents the average root mean square (RMS) noise of the *Euclid* and EXT images. This is computed from the `MerBksMosaic` RMS noise maps in ADU units, which are averaged and projected onto `HEALPix` maps. The resulting maps are stored as `DpdHealpixInfoMapVMPZ` products of information map type `Noise`. For unobserved regions, the RMS noise value is set to zero.

- Depth: represents the average depth at each sky position and is stored as `DpdHealpixDepthMapVMPZ` products. This is computed from the *Euclid* and EXT `MerBksMosaic` RMS maps according to the following definition:

$$m = -2.5 \log_{10}\left(\mathrm{RMS}\; d_{\rm thresh} \sqrt{\frac{A_{\rm aper}}{A_{\rm pixel}}}\right) + \mathrm{ZP}, \tag{3}$$

where RMS and ZP are the RMS noise value and photometric zero point, respectively, as defined in the `MerBksMosaic` maps. The detection threshold, $d_{\rm thresh}$, is set to 5, corresponding to a $5\,\sigma$ detection, while $A_{\rm aper}$ and $A_{\rm pixel}$ represent the detection aperture and pixel areas, respectively. A $2''$-diameter aperture is used to compute the depth.

- PSF FWHM: defines the average full width at half maximum (FWHM), in arcsec, at each sky position for the *Euclid* and EXT bands. This is stored in a DpdHealpixInfoMapVMPZ product of information map type `PSF`. For the `MerBksMosaic` maps, FWHM estimates are available only at the positions of bright stars in the tile field. A two-pass 2D interpolation (cubic spline then nearest-neighbour on the remaining not sampled areas) is therefore performed across the tile area, starting from a sufficiently coarse grid to avoid artefacts in the final derived mask.

- Bit mask: is an effective bit mask stored as a `DpdHealpixBitMaskVMPZ` product. For each `HEALPix` pixel in the final mask, it is computed by applying a bitwise `OR` operation to the bit-mask values of all `MerBksMosaic` pixels falling within it. The meaning of the different bits is described in the `MER` data model presented in Euclid Collaboration: Kümmel et al. (2026).

- Persistence: reflects the overall contamination of the NIR photometric data by persistence (see Euclid Collaboration: Kubik et al. 2026, for a detailed description of persistence effects) at each sky position. This is stored as a `DpdHealpixInfoMapVMPZ` product with information map type `Persistence`. The `HEALPix` persistence mask is derived from bit 13 of the `MerBksMosaic` bit mask, which flags regions severely affected by persistence. It ranges from 0 to 1 and gives the fraction of each `HEALPix` pixel affected by persistence, but does not provide information on the level of persistence.

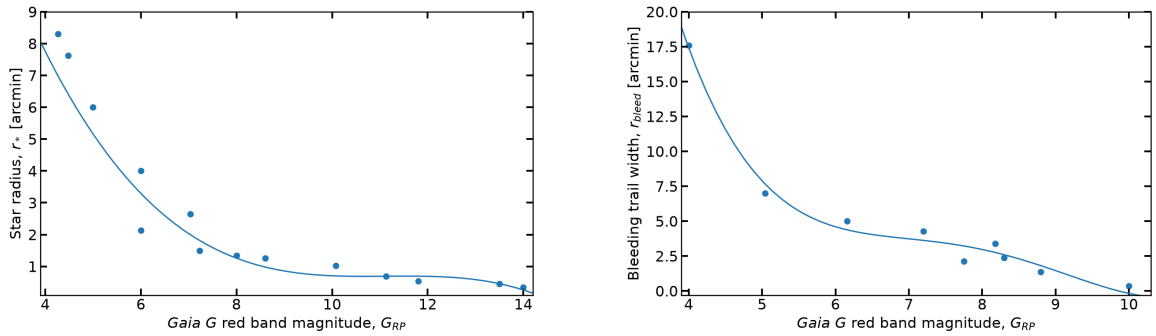


Fig. 1. *Left*: empirical radius around *Gaia* stars as a function of *Gaia* red band magnitude. *Right*: empirical bleeding-trail width around *Gaia* stars as a function of *Gaia* red band magnitude.

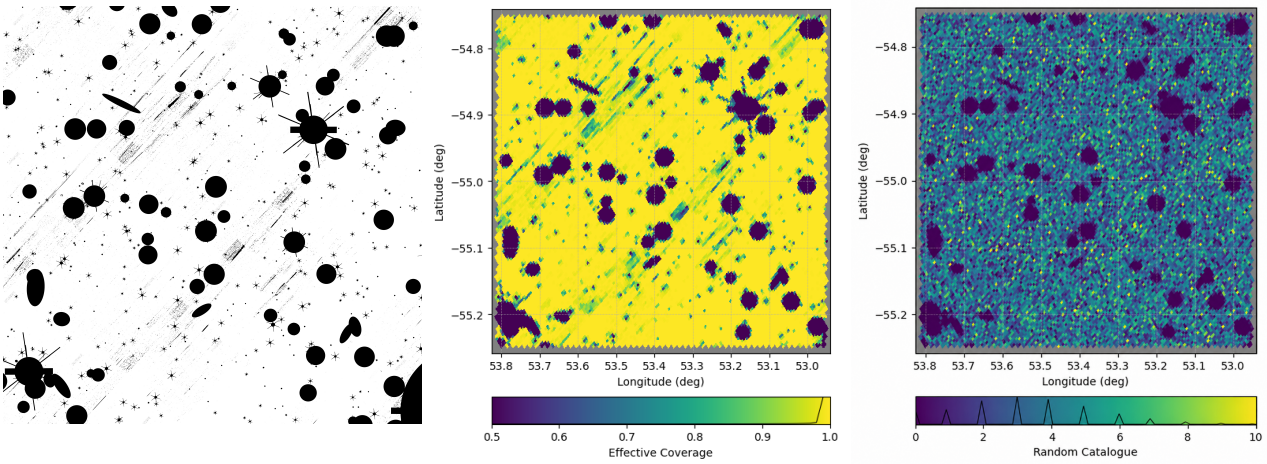


Fig. 2. *Left*: initial effective coverage binary mask at MER resolution for tile number 102015162. The circular masks around bright stars are clearly visible, as well as the additional masks for diffraction spikes and bleeding trails. *Middle*: final combined `HEALPix` effective coverage mask for the same tile. Because of the significantly lower resolution of the effective coverage mask, the original masking is smeared out, reducing the survey coverage. *Right*: example of random catalogue derived from the effective coverage mask for a fixed mean galaxy density of 80 galaxies arcmin^{-2}.

– NIR PRMS: represents the maximum RMS offset in milliarcseconds (mas) of the NIR stack astrometric residuals. The maximum RMS offset is computed for each stacked catalogue generated for a specific observation ID at a resolution of about 30″, following the procedure described in Euclid Collaboration: Radovich et al. (2026). The maps for all observation IDs corresponding to the EWS are then projected and averaged onto a common `HEALPix` grid. The resulting mask is stored as a `DpdHealpixInfoMapVMPZ` product with information map type `NIR_PRMS`.

– Pan-STARRS artefacts: defines regions in the Pan-STARRS *i*-band EXT images (see Euclid Collaboration: Corcho-Caballero et al. 2026) that are affected by systematic effects. This is stored as a `DpdHealpixInfoMapVMPZ` product with information map type `PanStarrsArtefacts`. The mask is built from the MER final catalogues (see Euclid Collaboration: Kümmel et al. 2026) by selecting sources with anomalous Pan-STARRS/VIS flux ratios, defined by default as $F_{\rm PS}/F_{\rm VIS} > 3.5$ or $F_{\rm PS}/F_{\rm VIS} < 1/3.5$, and requiring a flux-ratio signal-to-noise > 3. Their spatial distribution is smoothed with an Epanechnikov kernel density estimator[8] (KDE) with a 30″ bandwidth, evaluated on a regular 10″ RA–Dec grid. An adaptive density threshold derived from the KDE value distribution defines candidate contaminated regions, after which connected regions smaller than 30 grid pixels are discarded. The resulting binary mask is then projected onto a `HEALPix` grid, recording whether each `HEALPix` pixel is masked. This results into a binary mask.

[8] The Epanechnikov kernel density estimator is defined as $\hat{f}(x) = \frac{1}{nh}\sum_{i=1}^{n} K\left(\frac{x-x_i}{h}\right)$, where $K(u) = \frac{3}{4}(1-u^2)$ for $|u| \leq 1$ and 0 otherwise, n is the sample size, and h is the smoothing bandwidth.

3.4. Sky emission masks

Following the models presented in Euclid Collaboration: Scaramella et al. (2022), per-tile masks of zodiacal light emission and Galactic extinction are constructed for the *Euclid* bands.

– Galactic extinction: defines, for each sky position, the total extinction in magnitudes for each of the *Euclid* bands, as defined in equation 5 of Euclid Collaboration: Scaramella et al. (2022). This is stored as a `DpdHealpixInfoMapVMPZ` product with information map type `GalacticExtinction`.

– Zodiacal light: gives, for each sky position, the zodiacal light flux for each *Euclid* band normalised by the effective wavelength of the band, F/λ_*, as defined in table 4 of Euclid Collaboration: Scaramella et al. (2022). This is stored as a `DpdHealpixInfoMapVMPZ` product with information map type `ZodiacalLight`.

3.5. Star masks

The masks monitoring stellar density and flux across the sky are presented here. They are built by the *VMPZ_Star_Pipeline* using the `DpdExtGaiaCutout` products, which contain a reduced *Gaia* star catalogue for each tile. Only stars with a *Gaia* G-band flux above zero and a valid parallax angle are considered.

- Star number density: represents the number density of stars in each `HEALPix` pixel. This is stored as a `DpdHealpixInfoMapVMPZ` product with information map type `StarNumberDensity`.
- Mean star brightness: provides the mean flux of all stars lying within a given `HEALPix` pixel. This is stored as a `DpdHealpixInfoMapVMPZ` product with information map type `StarBrightnessMean`.
- Star brightness RMS: provides the RMS flux of all stars lying within a given `HEALPix` pixel. This is stored as a `DpdHealpixInfoMapVMPZ` product with information map type `StarBrightnessRms`.
- Star brightness standard deviation: provides the standard deviation of the flux of all stars lying within a given `HEALPix` pixel. this is stored as a `DpdHealpixInfoMapVMPZ` product with information map type `StarBrightnessStd`.

Examples for most of the masks are given in Appendix A and are discussed in Sect. 4.2.

4. EWS masks

4.1. Full survey masks

A subset of the DR1 EWS masks is shown in full-sky orthographic projection in Fig. 3, including the North (left hemisphere) and South (right hemisphere) regions. The effective coverage, presented in Fig. 3 (a), is crucial for scientific analyses to account for variations in sky coverage. Overall, the effective coverage is close to 1 (full coverage), except in regions around stars and near the edges of the coverage (see Fig. 2), which appear as blue dots in the figure. This is also clearly illustrated in Fig. 4, which displays the integrated coverage weighted area as a function of minimum selected coverage. The expected total area of the DR1 EWS is 2008.8 deg^2 (computed from the sum of the area of the regions for which we have one VIS exposure), of which 1642.4 deg^2 is preserved by the effective coverage mask. This effective area is obtained by summing the WEIGHT values in the effective coverage mask, multiplied by the `HEALPix` pixel area. Figure 3 also shows that the effective area for pixels with effective coverage above 0.8 corresponds to about 99% of the total effective area presented above. The orientation angles of the *Euclid* satellite are shown in Fig. 3 (b), (c), and (d). As expected, they are all within survey specifications. Moreover, the beta angle and the solar aspect angle are anti-correlated.

Figure 3 (e) shows that the VIS (I_E band) integration time is highly uniform across the survey, with only weak large-scale variations. This uniformity is expected from the survey design, such that most of the survey area is covered by 3- or 4-single-dither exposure (Euclid Collaboration: Tereno et al. 2026). Table 2 shows that the typical integration time values in the EWS are about 2735 and 338 for the VIS and NISP instruments, respectively. As a consequence, the VIS I_E RMS noise and depth masks also show small spatial variations across the survey. Similar conclusions can be drawn for the NISP bands. The left panel of Fig. 5 shows that the noise decreases as expected with increasing integration time. The 1D distribution of depth for the four *Euclid* bands is shown in the middle panel of Fig. 5. The distributions have narrow, well-defined peaks, with median depth values of 25.69, 24.14, 24.3, and 24.29 AB mag for the I_E, Y_E, J_E and H_E bands, respectively. The standard deviation is below 0.2 AB mag for all bands. A more detailed statistical description of the EWS RMS noise and depth distributions is also given in Table 2.

The EWS VIS PSF FWHM mask, which represents the VIS PSF FWHM, is shown in Fig. 3 (h). A very uniform spatial distribution is again observed. Similar results are obtained for the NISP bands. A statistical description of the 1D distribution of the PSF FWHM for the VIS and NISP bands is also given in Table 2. The median FWHM values are 0.″2, 0.″48, 0.″51, and 0.″56 for the I_E, Y_E, J_E, and H_E bands, respectively. The standard deviation of the spatial variation is below 0.″01.

4.2. High-resolution view

Additional examples of the EWS masks are presented in Appendix A for observation Patch ID 4. Figure A.1 shows the main survey masks, including the tile index, alpha angle, beta angle, solar aspect angle, and integration time for the four *Euclid* bands. The latter shows clear spatial patterns corresponding mainly to longer integration time in the overlap regions between adjacent tiles. These patterns are also reflected in the RMS noise and depth maps, as shown in Fig. A.3. This figure also presents the PSF FWHM, NIR PRMS, and persistence masks. The measured FWHM is larger in tile-overlap regions, where multiple exposures are combined. The NIR PRMS mask also shows these spatial variations with smaller NIR pointing RMS residuals in the overlapping regions. The persistence mask additionally exhibits tile-correlated structures, although they are less distinct and more difficult to interpret.

Finally, Fig. A.4 presents the main sky emission masks, including Galactic extinction, zodiacal light, star number density, mean star brightness, star brightness RMS, and star brightness standard deviation. Regions with larger stellar number density and mean brightness correspond to regions flagged on the effective coverage mask presented in Fig. A.3. This figure also shows the expected correlation between persistence and bright-star positions.

5. EDF masks

Figure 6 presents examples of the main VMPZ-ID photometric masks in the EDF-F (left panel), EDF-N, (middle panel), and EDF-S (right panel). The effective coverage masks clearly show fully masked regions (dark blue in the figure) due to star contamination, as discussed in previous sections. The integrated coverage weighted area is shown in the top panels of Fig. 7 for the three EDFs. Following the discussion in Sect. 4.1, the total (effective) observed area is 13.2 (11.8), 28.5 (21.1), and 33.0 (27.9) deg^2 for the EDF-F, EDF-N, and EDF-S, respectively. Thus, the effective coverage mask preserves 89.3, 74.0, and 84.5% of this area. Furthermore, 75, 72, and 92% of the preserved regions have effective coverage greater than 0.8.

Figure 6 also shows that the I_E integration time has small spatial variations for EDF-N and EDF-S, while more significant structure is observed for EDF-F. This can be explained by the

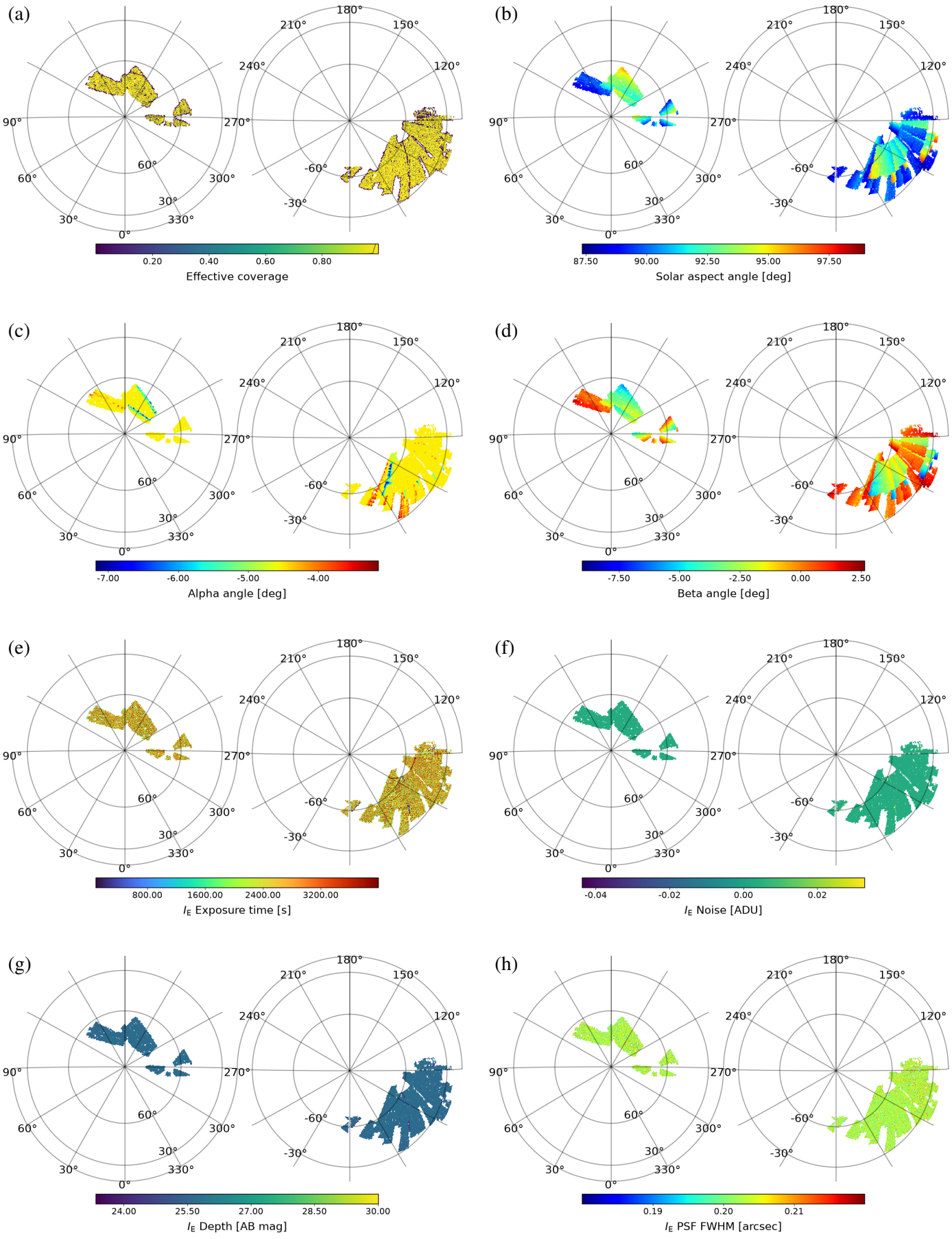


Fig. 3. DR1 EWS, full-sky orthographic projections of a selection of the VMPZ-ID masks including: (a) effective coverage; (b) solar aspect angle; (c) alpha angle; (d) beta angle; (e) VIS integration time; (f) VIS RMS noise; (g) VIS depth; and (h) VIS PSF FWHM.

Table 2. DR1 EWS mean, median, standard deviation, and percentiles of the distributions of integration time, RMS noise, depth, and PSF FWHM for the four *Euclid* bands.

Band	Quantity	Mean	Median	Std	Q_{16}	Q_{25}	Q_{75}	Q_{84}	IQR[a]
I_E	Exposures [s]	2735	2421	922	1861	2332	3071	3632	740
	Noise [ADU]	0.003882	0.003716	0.001423	0.003238	0.003421	0.004085	0.004239	0.0006632
	Depth [AB mag]	25.68	25.69	0.224	25.56	25.59	25.78	25.84	0.186
	PSF FWHM [arcsec]	0.2029	0.2028	0.004051	0.1991	0.2004	0.2053	0.2066	0.004964
Y_E	Exposures [s]	338	349	117	262	262	349	436	87
	Noise [ADU]	2.089	2.077	0.4039	1.794	1.867	2.253	2.333	0.3855
	Depth [AB mag]	24.15	24.14	0.1699	24.01	24.05	24.25	24.3	0.2038
	PSF FWHM [arcsec]	0.4879	0.4883	0.01016	0.4791	0.4825	0.4939	0.4968	0.01142
J_E	Exposures [s]	338	349	118	262	262	349	436	87
	Noise [ADU]	2.393	2.379	0.4584	2.057	2.139	2.574	2.67	0.4349
	Depth [AB mag]	24.3	24.29	0.1717	24.16	24.2	24.41	24.45	0.2009
	PSF FWHM [arcsec]	0.5138	0.5143	0.01071	0.5045	0.5081	0.5201	0.5232	0.01206
H_E	Exposures [s]	339	349	117	262	262	349	436	87
	Noise [ADU]	2.194	2.183	0.4215	1.887	1.963	2.364	2.45	0.4013
	Depth [AB mag]	24.29	24.28	0.1704	24.16	24.2	24.4	24.44	0.202
	PSF FWHM [arcsec]	0.5589	0.5593	0.009184	0.5512	0.5542	0.5642	0.5666	0.009917

Notes. [a] Interquartile range $\equiv Q_{75} - Q_{25}$.

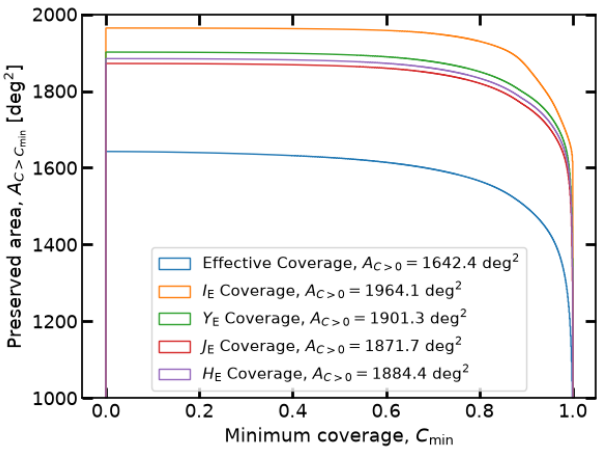


Fig. 4. For DR1 EWS, the integrated coverage weighted area $A_{C>C_{min}}$ for `HEALPix` pixels with coverage above a given minimum value, C_{min}. This is shown for the effective coverage mask and the individual coverage masks for the four *Euclid* bands. We recall that the effective coverage also includes the EXT data.

significantly larger number of exposures and multiple exposure angles in EDF-N and EDF-S compared with EDF-F. A similar behaviour is observed for the I_E and H_E depth masks. This is also visible in the bottom panel of Fig. 7, where the 1D depth distributions are shown for the four *Euclid* bands and the three EDFs. A detailed statistical description of these distributions is given in Tables B.1, B.2, and B.3. The median I_E depth (integration time) values in AB mag (seconds) are 25.93 (4842), 26.91 (25 330), and 26.85 (23 560) for EDF-F, EDF-N, and EDF-S, respectively. These values are consistent with the corresponding numbers of visits, namely 2, 11, and 10 (Euclid Collaboration: Tereno et al. 2026).

6. Summary and conclusions

In this paper, a series of photometric masks has been presented in the form of `HEALPix` maps at a resolution of $N_{side} = 16\,384$ for each tile of the DR1 EWS and EDS. These masks were built using the OU-LE3 VMPZ-ID PF and pipelines within the *Euclid* SGS. They represent spatial variations in the observational properties across the DR1 survey (integration time and satellite position angles), the instrumental properties for the *Euclid* and EXT bands (coverage, instrumental noise and depth, PSF width, systematic flags, NIR persistence, and astrometric uncertainties), foreground sky emission (Galactic extinction and zodiacal light), and the stellar distribution (star number density and star flux properties).

A mask representing the overall effective coverage of DR1 and combining information from the *Euclid* and EXT bands is also provided. This mask also accounts for bright-star contamination, including diffraction spikes and bleeding effects in the *Euclid* and EXT images. Overall, the effective coverage mask reduces the available area by 18.1% in the DR1 EWS and by 11 to 26% in the EDFs. Nevertheless, the effective coverage mask should be used to avoid spurious objects and artefacts in the data when selecting Euclid DR1 photometric galaxy samples for scientific analyses.

The instrumental performance in the VIS and NISP photometric bands is very stable across the survey. Spatial variations in instrumental RMS roise are strongly correlated with integration time, as expected. For the DR1 EWS, the standard deviation of depth (for a 2″ aperture) is below 0.2 AB mag, with median values of 25.69, 24.14, 24.3, and 24.29 for the I_E, Y_E, J_E, and H_E bands, respectively. Furthermore, the spatial standard deviations of the PSF FWHM are of the order of 0.″01, with median values of 0.″2, 0.″48, 0.″51, and 0.″56 for the I_E, Y_E, J_E, and H_E bands, respectively. At small angular scales, however, some structured patterns in integration time are observed.

For the DR1 EDS, multiple visits at different observation angles tend to smooth out spatial variations in the instrumental properties, particularly in EDF-N and EDF-S. Median depth values of 26.91, 25.30, 25.44, and 25.45 are achieved for the I_E, Y_E, J_E, and H_E bands, respectively. The standard deviation of depth is below 0.16, 0.44, and 0.40 AB mag for EDF-F, EDF-N, and EDF-S, respectively.

The VMPZ-ID photometric masks will be particularly relevant for forthcoming *Euclid* photometric astrophysical and cosmological analyses. They will be key for monitoring and correcting potential systematic spatial variations in galaxy number density, which could otherwise bias important derived quantities, such as cosmological parameter estimates.

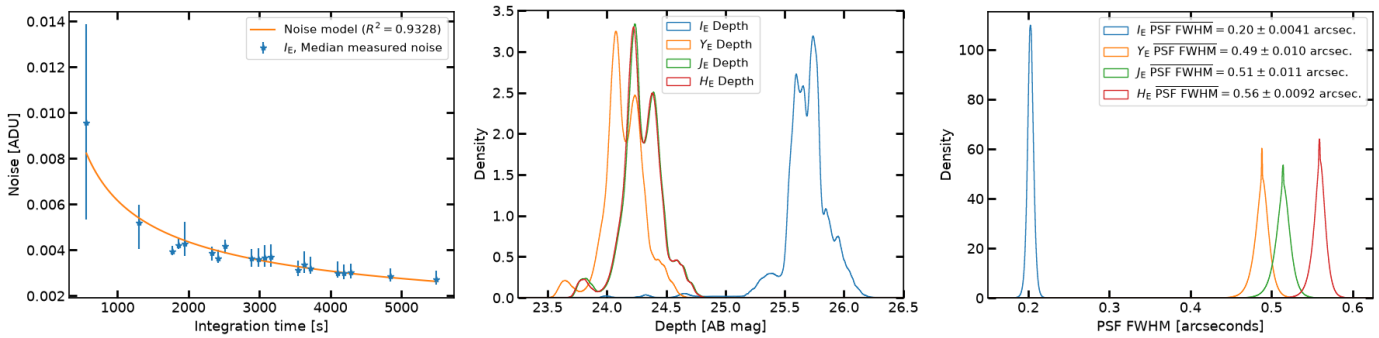


Fig. 5. For DR1 EWS, the panels show, from left to right: the VIS RMS noise as a function of integration time, fitted with $\sigma(t) = \sqrt{A\, t_{\rm ref}/t + B}$, where A is the exposure-dependent variance at the reference integration time $t_{\rm ref}$ and B is the exposure-independent term, with R^2 denoting the coefficient of determination of the fit; and the 1D distributions of depth and PSF FWHM for the four *Euclid* bands.

Acknowledgements. The Euclid Consortium acknowledges the European Space Agency and a number of agencies and institutes that have supported the development of *Euclid*, in particular the Agenzia Spaziale Italiana, the Austrian Forschungsförderungsgesellschaft funded through BMIMI, the Belgian Science Policy, the Canadian Euclid Consortium, the Deutsches Zentrum für Luft- und Raumfahrt, the DTU Space and the Niels Bohr Institute in Denmark, the French Centre National d'Etudes Spatiales, the Fundação para a Ciência e a Tecnologia, the Hungarian Academy of Sciences, the Ministerio de Ciencia, Innovación y Universidades, the National Aeronautics and Space Administration, the National Astronomical Observatory of Japan, the Netherlandse Onderzoekschool Voor Astronomie, the Norwegian Space Agency, the Research Council of Finland, the Romanian Space Agency, the Swiss Space Office (SSO) at the State Secretariat for Education, Research, and Innovation (SERI), and the United Kingdom Space Agency. A complete and detailed list is available on the *Euclid* web site (www.euclid-ec.org/consortium/community/). This work has made use of the Euclid Data Release 1 (DR1) from the European Space Agency (ESA) mission *Euclid*, available at https://www.cosmos.esa.int/web/euclid/data-release-dr1.

References

Abbott, T. M. C., Adamów, M., Aguena, M., et al. 2021, ApJS, 255, 20
Aihara, H., Arimoto, N., Armstrong, R., et al. 2018, PASJ, 70, S4
Amendola, L., Appleby, S., Avgoustidis, A., et al. 2018, Living Reviews in Relativity, 21, 2
Desai, S., Mohr, J., Bertin, E., Kümmel, M., & Wetzstein, M. 2016, Astronomy and Computing, 16, 67
Euclid Collaboration: Aussel, H., Tereno, I., Schirmer, M., et al. 2026a, A&A, 711, A1
Euclid Collaboration: Aussel, H. et al. 2026b, arXiv, submitted
Euclid Collaboration: Blanchard, A., Camera, S., Carbone, C., et al. 2020, A&A, 642, A191
Euclid Collaboration: Corcho-Caballero, P., Balbinot, E., De Jong, J., et al. 2026, A&A, submitted
Euclid Collaboration: Cropper, M., Al-Bahlawan, A., Amiaux, J., et al. 2025, A&A, 697, A2
Euclid Collaboration: Hartley, W., Paltani, S., Dubath, F., et al. 2026, A&A, submitted
Euclid Collaboration: Jahnke, K., Gillard, W., Schirmer, M., et al. 2025, A&A, 697, A3
Euclid Collaboration: Kubik, B., Conseil, S., Ferriol, S., et al. 2026, A&A, submitted
Euclid Collaboration: Kümmel, M., Caro, F., Dimauro, P., et al. 2026, A&A, submitted
Euclid Collaboration: Mellier, Y., Abdurro'uf, Acevedo Barroso, J., et al. 2025, A&A, 697, A1
Euclid Collaboration: Radovich, M., da Silva, R., Polenta, G., et al. 2026, A&A, submitted
Euclid Collaboration: Ruffenach, M., Frailis, M., Zacchei, A., et al. 2026, A&A, submitted
Euclid Collaboration: Scaramella, R., Amiaux, J., Mellier, Y., et al. 2022, A&A, 662, A112
Euclid Collaboration: Tereno, I., Dinis, J., Dupac, X., et al. 2026, arXiv, submitted
Euclid Data Release 1. 2026, https://doi.org/10.57780/esa-d079c51
Gaia Collaboration, Prusti, T., de Bruijne, J. H. J., et al. 2016, A&A, 595, A1
Górski, K. M., Hivon, E., Banday, A. J., et al. 2005, ApJ, 622, 759
Ibata, R. A., McConnachie, A., Cuillandre, J.-C., et al. 2017, ApJ, 848, 128
Magnier, E. A., Schlafly, E. F., Finkbeiner, D. P., et al. 2020, ApJS, 251, 6
Weaverdyck, N., Rodríguez-Monroy, M., Elvin-Poole, J., et al. 2026, arXiv e-prints, arXiv:2601.14484
Yan, Z., Wright, A. H., Chisari, N. E., et al. 2025, A&A, 694, A259

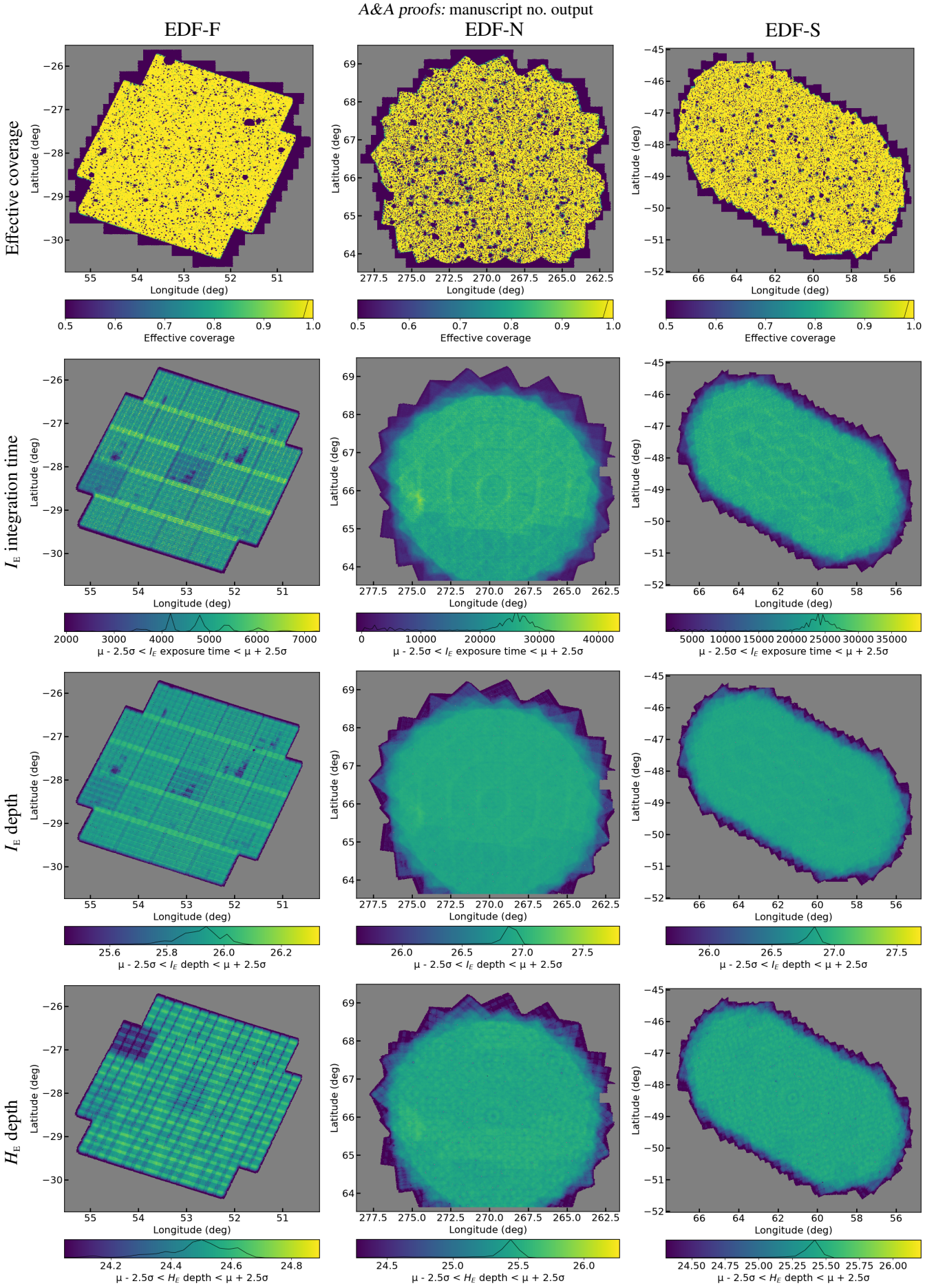


Fig. 6. Examples of VMPZ-ID photometric masks for the EDF-F (left), EDF-N (middle), and EDF-S (right). From top to bottom, the panels show the effective coverage, integration time and depth for I_E, and the depth for H_E.

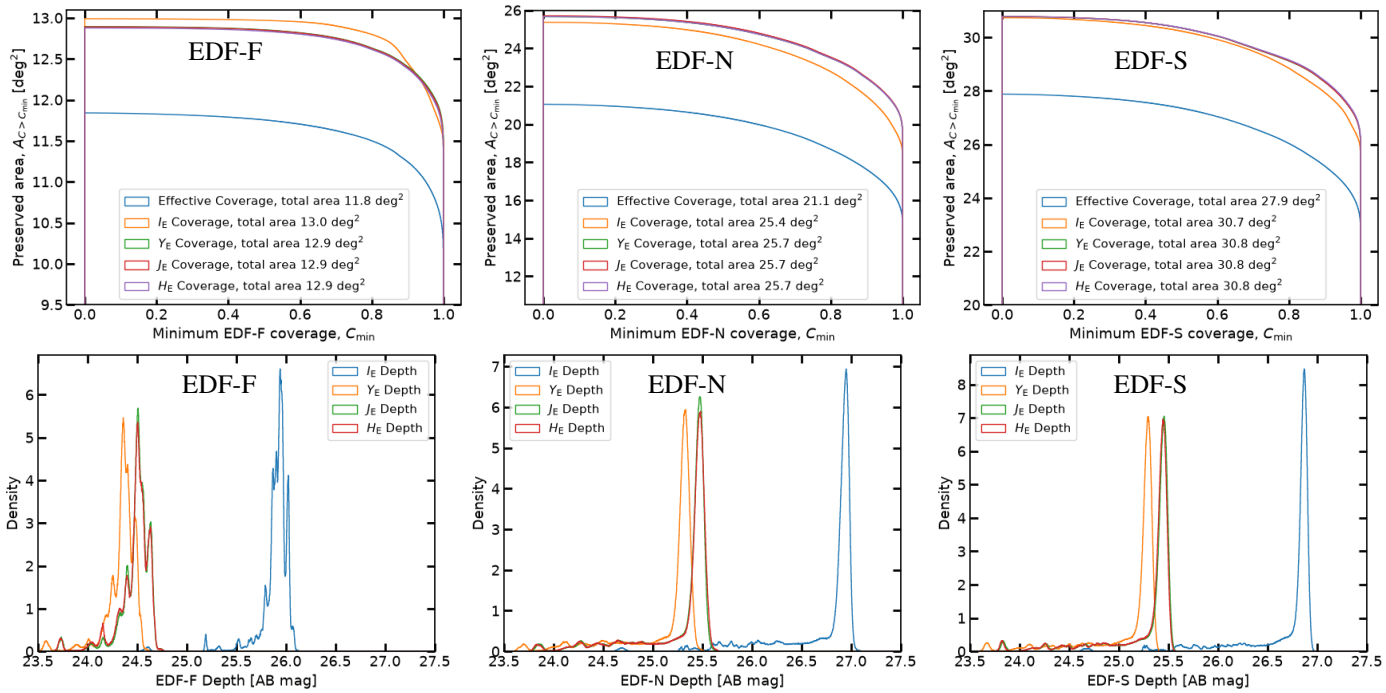


Fig. 7. *Top*: integrated coverage weighted area $A_{C>C_{\rm min}}$ for `HEALPix` pixels with coverage above a given minimum value, $C_{\rm min}$. *Bottom*: depth distributions for the four *Euclid* bands. From left to right results for the EDF-F, EDF-N, and EDF-S regions are presented.

Authors and affiliations

Euclid Collaboration: J. Odier[⋆1], J. F. Macias-Perez[1], G. Alguero[1], C. Benoist[2], M. Radovich[3], P. Corcho-Caballero[4], H. Aussel[5], P. Casenove[6], M. Ruffenach[6], S. Farrens[5], B. Kubik[7], M. Kümmel[8], S. Andreon[9], C. Baccigalupi[10,11,12,13], M. Baldi[14,15,16], A. Balestra[3], S. Bardelli[15], P. Battaglia[15], A. Biviano[11,10], M. Bolzonella[15], E. Branchini[17,18,9], M. Brescia[19,20], J. Brinchmann[21,22,23], S. Camera[24,25,26], G. Cañas-Herrera[27], V. Capobianco[26], C. Carbone[28], F. J. Castander[29,30], M. Castellano[31], G. Castignani[15], S. Cavuoti[20,32], A. Cimatti[33], G. Congedo[34], L. Conversi[35,36], Y. Copin[7], A. Costille[37], M. Cropper[38], A. Da Silva[39,40], R. da Silva[31,41], G. De Lucia[11], X. Dupac[36], S. Escoffier[42], M. Farina[43], R. Farinelli[15], S. Ferriol[7], S. Fotopoulou[44], N. Fourmanoit[42], M. Frailis[11], L. Gabarra[45], S. Galeotta[11], K. George[46], C. Giocoli[15,16], F. Grupp[47,8], L. Guzzo[48,9,49], W. G. Hartley[50], S. V. H. Haugan[51], S. Hemmati[52], H. Hoekstra[27], F. Hormuth[53], K. Jahnke[54], M. Jhabvala[55], S. Kermiche[42], A. Kiessling[56], M. Kunz[57], H. Kurki-Suonio[58,59], P. Liebing[38], S. Ligori[26], P. B. Lilje[51], I. Lloro[60], M. Magliocchetti[43], O. Marggraf[61], M. Martinelli[31,62], N. Martinet[37], R. J. Massey[63], N. Mauri[33,16], H. J. McCracken[64], E. Medinaceli[15], M. Meneghetti[15,16], E. Merlin[3], G. Meylan[65], P. Monaco[66,11,12,10], M. Moresco[67,15], L. Moscardini[67,15,16], R. Nakajima[61], C. Neissner[68,69], R. C. Nichol[70], S.-M. Niemi[71], C. Padilla[68], F. Pasian[11], J. A. Peacock[34], W. J. Percival[72,73,74], V. Pettorino[71], S. Pires[5], G. Polenta[41], M. Poncet[6], L. A. Popa[75], L. Pozzetti[15], A. Refregier[76], A. Renzi[77,78,15], J. Rhodes[56], G. Riccio[20], E. Romelli[11], M. Roncarelli[15], B. Rusholme[52], R. Saglia[8,47], Z. Sakr[79,80,81], M. Schirmer[54], P. Schneider[61], A. Secroun[42], E. Sihvola[58,59], P. Simon[61], C. Sirignano[77,78], G. Sirri[16], J. Skottfelt[82], L. Stanco[78], P. Tallada-Crespí[83,69], H. I. Teplitz[84], I. Tereno[39,40], N. Tessore[38], S. Toft[85,86], R. Toledo-Moreo[87,88], I. Tutusaus[29,30,80], J. Valiviita[58,59], T. Vassallo[11,46], A. Veropalumbo[9,18,17], Y. Wang[52], J. Weller[8,47], A. Zacchei[11,10], G. Zamorani[15], F. M. Zerbi[9], E. Zucca[15], V. Allevato[20], M. Ballardini[89,90,15], S. Borgani[66,10,11,12,91], E. Bozzo[50], C. Burigana[92,93], M. Calabrese[94,28], F. Caro[31], T. Castro[95,11,10], S. Conseil[96,7], D. Di Ferdinando[16], J. A. Escartin Vigo[47], G. Fabbian[97], T. Gasparetto[31], A. Gregorio[66,11,12], C. M. Gutierrez[98,99], Y. Kang[100], A. Loureiro[101,102], R. Maoli[103,31], R. B. Metcalf[67,15], M. Pöntinen[58], E. Sarpa[11], V. Scottez[104,105], M. Sereno[15,16], K. Tanidis[106], M. Tenti[16], M. Wiesmann[51], Abdurro'uf[107], J. A. Acevedo Barroso[56], Y. Akrami[79,108], G. Angora[20,89], S. Anselmi[78,77,109], M. Archidiacono[48,49], G. Aricò[16], F. Atrio-Barandela[110], M. Aubert[7], M. Baes[111], N. Bartolo[77,78,3], L. Bazzanini[92,89], J. R. Bermejo-Climent[112,113], D. Bertacca[77,3,78], M. Bethermin[114], F. Bouchè[115,32], A. Calabro[31], C. S. Carvalho[116], N. Chartab[52], F. Cogato[15], T. E. Collett[117], M. Correnti[31,41], B. Csizi[100], O. Cucciati[15], T. de Boer[118], G. Desprez[4], A. Díaz-Sánchez[119], S. Di Domizio[17,18], V. Duret[120], A. Enia[121,15], A. Farina[9,18], A. Fontana[31], A. Franco[122,123,124], N. Frusciante[125,126], A. Fumagalli[11], Y. Fu[27,4], K. Ganga[127], R. Gavazzi[37,64], E. Gaztanaga[29,30,117], Z. Ghaffari[11,10], F. Gianotti[15], G. Gozaliasl[128,58], M. Guidi[14,15], H. Hildebrandt[129], J. Hjorth[130], D. Karagiannis[131,89,132], J. Kim[45], C. C. Kirkpatrick[133], A. Kovács[113,112], I. Kovačić[111], K. Koyama[117], S. Kruk[36], M. C. Lam[34], M. Lembo[64], M. D. Lepinzan[11], L. Linke[100], F. Mannucci[134], C. J. A. P. Martins[135,22], M. Migliaccio[136,137], M. Miluzio[36,138], G. Morgante[15], K. Naidoo[117,54], A. Navarro-Alsina[61], S. Nesseris[79], L. Nicastro[15], F. Oppizzi[18,78,77], F. Pace[24,25,26,40], M. J. Page[38], D. Paoletti[15,93], F. Passalacqua[78], K. Paterson[54], C. Pattison[117], A. Pisani[42], L. Pizzuti[139], J. J. Popp[140], D. Potter[141], M. Poulain[142], G. W. Pratt[5], S. Quai[67,15], F. Ricci[143,31], G. Rodighiero[77,3], W. Roster[47], M. Sahlén[144], D. B. Sanders[118], A. Schneider[141], S. Serjeant[140], L. C. Smith[145], E. Soubrie[97], I. Szapudi[118], G. Testera[18], R. Teyssier[146], S. Tosi[17,9,18], C. Uhlemann[147], C. Valieri[16], A. Viitanen[50,133,31], S. Vinciguerra[37], M. von Wietersheim-Kramsta[63,148], and D. Scott[149]

[1] Univ. Grenoble Alpes, CNRS, Grenoble INP, LPSC-IN2P3, 53, Avenue des Martyrs, 38000 Grenoble, France
[2] Université Côte d'Azur, Observatoire de la Côte d'Azur, CNRS, Laboratoire Lagrange, Bd de l'Observatoire, CS 34229, 06304 Nice cedex 4, France
[3] INAF-Osservatorio Astronomico di Padova, Via dell'Osservatorio 5, 35122 Padova, Italy
[4] Kapteyn Astronomical Institute, University of Groningen, PO Box 800, 9700 AV Groningen, The Netherlands
[5] Université Paris-Saclay, Université Paris Cité, CEA, CNRS, AIM, 91191, Gif-sur-Yvette, France
[6] Centre National d'Etudes Spatiales – Centre spatial de Toulouse, 18 avenue Edouard Belin, 31401 Toulouse Cedex 9, France
[7] Université Lyon 1, CNRS/IN2P3, IP2I Lyon, Villeurbanne, France
[8] Universitäts-Sternwarte München, Fakultät für Physik, Ludwig-Maximilians-Universität München, Scheinerstr. 1, 81679 München, Germany
[9] INAF-Osservatorio Astronomico di Brera, Via Brera 28, 20122 Milano, Italy
[10] IFPU, Institute for Fundamental Physics of the Universe, via Beirut 2, 34151 Trieste, Italy
[11] INAF-Osservatorio Astronomico di Trieste, Via G. B. Tiepolo 11, 34143 Trieste, Italy
[12] INFN, Sezione di Trieste, Via Valerio 2, 34127 Trieste TS, Italy
[13] SISSA, International School for Advanced Studies, Via Bonomea 265, 34136 Trieste TS, Italy
[14] Dipartimento di Fisica e Astronomia, Università di Bologna, Via Gobetti 93/2, 40129 Bologna, Italy
[15] INAF-Osservatorio di Astrofisica e Scienza dello Spazio di Bologna, Via Piero Gobetti 93/3, 40129 Bologna, Italy
[16] INFN-Sezione di Bologna, Viale Berti Pichat 6/2, 40127 Bologna, Italy

[17] Dipartimento di Fisica, Università di Genova, Via Dodecaneso 33, 16146, Genova, Italy
[18] INFN-Sezione di Genova, Via Dodecaneso 33, 16146, Genova, Italy
[19] Department of Physics "E. Pancini", University Federico II, Via Cinthia 6, 80126, Napoli, Italy
[20] INAF-Osservatorio Astronomico di Capodimonte, Via Moiariello 16, 80131 Napoli, Italy
[21] European Southern Observatory, Karl-Schwarzschild-Str. 2, 85748 Garching, Germany
[22] Instituto de Astrofísica e Ciências do Espaço, Universidade do Porto, CAUP, Rua das Estrelas, PT4150-762 Porto, Portugal
[23] Faculdade de Ciências da Universidade do Porto, Rua do Campo de Alegre, 4150-007 Porto, Portugal
[24] Dipartimento di Fisica, Università degli Studi di Torino, Via P. Giuria 1, 10125 Torino, Italy
[25] INFN-Sezione di Torino, Via P. Giuria 1, 10125 Torino, Italy
[26] INAF-Osservatorio Astrofisico di Torino, Via Osservatorio 20, 10025 Pino Torinese (TO), Italy
[27] Leiden Observatory, Leiden University, Einsteinweg 55, 2333 CC Leiden, The Netherlands
[28] INAF-IASF Milano, Via Alfonso Corti 12, 20133 Milano, Italy
[29] Institute of Space Sciences (ICE, CSIC), Campus UAB, Carrer de Can Magrans, s/n, 08193 Barcelona, Spain
[30] Institut d'Estudis Espacials de Catalunya (IEEC), Edifici RDIT, Campus UPC, 08860 Castelldefels, Barcelona, Spain
[31] INAF-Osservatorio Astronomico di Roma, Via Frascati 33, 00078 Monteporzio Catone, Italy
[32] INFN – Sezione di Napoli, Via Cinthia 6, 80126, Napoli, Italy
[33] Dipartimento di Fisica e Astronomia "Augusto Righi" - Alma Mater Studiorum Università di Bologna, Viale Berti Pichat 6/2, 40127 Bologna, Italy
[34] Institute for Astronomy, University of Edinburgh, Royal Observatory, Blackford Hill, Edinburgh EH9 3HJ, UK
[35] European Space Agency/ESRIN, Largo Galileo Galilei 1, 00044 Frascati, Roma, Italy
[36] ESAC/ESA, Camino Bajo del Castillo, s/n., Urb. Villafranca del Castillo, 28692 Villanueva de la Cañada, Madrid, Spain
[37] Aix-Marseille Université, CNRS, CNES, LAM, Marseille, France
[38] Mullard Space Science Laboratory, University College London, Holmbury St Mary, Dorking, Surrey RH5 6NT, UK
[39] Departamento de Física, Faculdade de Ciências, Universidade de Lisboa, Edifício C8, Campo Grande, PT1749-016 Lisboa, Portugal
[40] Instituto de Astrofísica e Ciências do Espaço, Faculdade de Ciências, Universidade de Lisboa, Campo Grande, 1749-016 Lisboa, Portugal
[41] Space Science Data Center, Italian Space Agency, via del Politecnico snc, 00133 Roma, Italy
[42] Aix-Marseille Université, CNRS/IN2P3, CPPM, Marseille, France
[43] INAF-Istituto di Astrofisica e Planetologia Spaziali, via del Fosso del Cavaliere, 100, 00100 Roma, Italy
[44] School of Physics, HH Wills Physics Laboratory, University of Bristol, Tyndall Avenue, Bristol, BS8 1TL, UK
[45] Department of Physics, University of Oxford, Keble Road, Oxford OX1 3RH, UK
[46] University Observatory, LMU Faculty of Physics, Scheinerstr. 1, 81679 Munich, Germany
[47] Max Planck Institute for Extraterrestrial Physics, Giessenbachstr. 1, 85748 Garching, Germany
[48] Dipartimento di Fisica "Aldo Pontremoli", Università degli Studi di Milano, Via Celoria 16, 20133 Milano, Italy
[49] INFN-Sezione di Milano, Via Celoria 16, 20133 Milano, Italy
[50] Department of Astronomy, University of Geneva, ch. d'Ecogia 16, 1290 Versoix, Switzerland
[51] Institute of Theoretical Astrophysics, University of Oslo, P.O. Box 1029 Blindern, 0315 Oslo, Norway
[52] Caltech/IPAC, 1200 E. California Blvd., Pasadena, CA 91125, USA
[53] Felix Hormuth Engineering, Goethestr. 17, 69181 Leimen, Germany
[54] Max-Planck-Institut für Astronomie, Königstuhl 17, 69117 Heidelberg, Germany
[55] NASA Goddard Space Flight Center, Greenbelt, MD 20771, USA
[56] Jet Propulsion Laboratory, California Institute of Technology, 4800 Oak Grove Drive, Pasadena, CA, 91109, USA
[57] Université de Genève, Département de Physique Théorique and Centre for Astroparticle Physics, 24 quai Ernest-Ansermet, CH-1211 Genève 4, Switzerland
[58] Department of Physics, P.O. Box 64, University of Helsinki, 00014 Helsinki, Finland
[59] Helsinki Institute of Physics, Gustaf Hällströmin katu 2, University of Helsinki, 00014 Helsinki, Finland
[60] SKAO, Jodrell Bank, Lower Withington, Macclesfield SK11 9FT, UK
[61] Universität Bonn, Argelander-Institut für Astronomie, Auf dem Hügel 71, 53121 Bonn, Germany
[62] INFN-Sezione di Roma, Piazzale Aldo Moro, 2 - c/o Dipartimento di Fisica, Edificio G. Marconi, 00185 Roma, Italy
[63] Department of Physics, Institute for Computational Cosmology, Durham University, South Road, Durham, DH1 3LE, UK
[64] Institut d'Astrophysique de Paris, UMR 7095, CNRS, and Sorbonne Université, 98 bis boulevard Arago, 75014 Paris, France
[65] Institute of Physics, Laboratory of Astrophysics, Ecole Polytechnique Fédérale de Lausanne (EPFL), Observatoire de Sauverny, 1290 Versoix, Switzerland
[66] Dipartimento di Fisica - Sezione di Astronomia, Università di Trieste, Via Tiepolo 11, 34131 Trieste, Italy
[67] Dipartimento di Fisica e Astronomia "Augusto Righi" - Alma Mater Studiorum Università di Bologna, via Piero Gobetti 93/2, 40129 Bologna, Italy
[68] Institut de Física d'Altes Energies (IFAE), The Barcelona Institute of Science and Technology, Campus UAB, 08193 Bellaterra (Barcelona), Spain
[69] Port d'Informació Científica, Campus UAB, C. Albareda s/n, 08193 Bellaterra (Barcelona), Spain
[70] School of Mathematics and Physics, University of Surrey, Guildford, Surrey, GU2 7XH, UK
[71] European Space Agency/ESTEC, Keplerlaan 1, 2201 AZ Noordwijk, The Netherlands
[72] Waterloo Centre for Astrophysics, University of Waterloo, Waterloo, Ontario N2L 3G1, Canada
[73] Department of Physics and Astronomy, University of Waterloo, Waterloo, Ontario N2L 3G1, Canada
[74] Perimeter Institute for Theoretical Physics, Waterloo, Ontario N2L 2Y5, Canada
[75] Institute of Space Science, Str. Atomistilor, nr. 409 Măgurele, Ilfov, 077125, Romania
[76] Institute for Particle Physics and Astrophysics, Dept. of Physics, ETH Zurich, Wolfgang-Pauli-Strasse 27, 8093 Zurich, Switzerland
[77] Dipartimento di Fisica e Astronomia "G. Galilei", Università di Padova, Via Marzolo 8, 35131 Padova, Italy
[78] INFN-Padova, Via Marzolo 8, 35131 Padova, Italy
[79] Instituto de Física Teórica UAM-CSIC, Campus de Cantoblanco, 28049 Madrid, Spain
[80] Institut de Recherche en Astrophysique et Planétologie (IRAP), Université de Toulouse, CNRS, UPS, CNES, 14 Av. Edouard Belin, 31400 Toulouse, France

[81] Université St Joseph; Faculty of Sciences, Beirut, Lebanon
[82] Centre for Electronic Imaging, Open University, Walton Hall, Milton Keynes, MK7 6AA, UK
[83] Centro de Investigaciones Energéticas, Medioambientales y Tecnológicas (CIEMAT), Avenida Complutense 40, 28040 Madrid, Spain
[84] Infrared Processing and Analysis Center, California Institute of Technology, Pasadena, CA 91125, USA
[85] Cosmic Dawn Center (DAWN)
[86] Niels Bohr Institute, University of Copenhagen, Jagtvej 128, 2200 Copenhagen, Denmark
[87] Universidad Politécnica de Cartagena, Departamento de Electrónica y Tecnología de Computadoras, Plaza del Hospital 1, 30202 Cartagena, Spain
[88] European University of Technology EUt+, European Union
[89] Dipartimento di Fisica e Scienze della Terra, Università degli Studi di Ferrara, Via Giuseppe Saragat 1, 44122 Ferrara, Italy
[90] Istituto Nazionale di Fisica Nucleare, Sezione di Ferrara, Via Giuseppe Saragat 1, 44122 Ferrara, Italy
[91] ICSC - Centro Nazionale di Ricerca in High Performance Computing, Big Data e Quantum Computing, Via Magnanelli 2, Bologna, Italy
[92] INAF, Istituto di Radioastronomia, Via Piero Gobetti 101, 40129 Bologna, Italy
[93] INFN-Bologna, Via Irnerio 46, 40126 Bologna, Italy
[94] Astronomical Observatory of the Autonomous Region of the Aosta Valley (OAVdA), Loc. Lignan 39, I-11020, Nus (Aosta Valley), Italy
[95] Department of Mathematical Physics, Institute of Physics, University of São Paulo, R. do Matão 1371, 05508-090, São Paulo, SP, Brazil
[96] Centre de Recherche Astrophysique de Lyon, UMR5574, CNRS, Université Claude Bernard Lyon 1, ENS de Lyon, 69230, Saint-Genis-Laval, France
[97] Université Paris-Saclay, CNRS, Institut d'astrophysique spatiale, 91405, Orsay, France
[98] Instituto de Astrofísica de Canarias, E-38205 La Laguna, Tenerife, Spain
[99] Universidad de La Laguna, Dpto. Astrofísica, E-38206 La Laguna, Tenerife, Spain
[100] Universität Innsbruck, Institut für Astro- und Teilchenphysik, Technikerstr. 25/8, 6020 Innsbruck, Austria
[101] Oskar Klein Centre for Cosmoparticle Physics, Department of Physics, Stockholm University, Stockholm, SE-106 91, Sweden
[102] Astrophysics Group, Blackett Laboratory, Imperial College London, London SW7 2AZ, UK
[103] Dipartimento di Fisica, Sapienza Università di Roma, Piazzale Aldo Moro 2, 00185 Roma, Italy
[104] Institut d'Astrophysique de Paris, 98bis Boulevard Arago, 75014, Paris, France
[105] ICL, Junia, Université Catholique de Lille, LITL, 59000 Lille, France
[106] Center for Astrophysics and Cosmology, University of Nova Gorica, Nova Gorica, Slovenia
[107] Department of Astronomy, Indiana University, 727 East Third Street, Bloomington, IN 47405, USA
[108] CERCA/ISO, Department of Physics, Case Western Reserve University, 10900 Euclid Avenue, Cleveland, OH 44106, USA
[109] Laboratoire Univers et Théorie, Observatoire de Paris, Université PSL, Université Paris Cité, CNRS, 92190 Meudon, France
[110] Departamento de Física Fundamental. Universidad de Salamanca. Plaza de la Merced s/n. 37008 Salamanca, Spain
[111] Universiteit Gent, Department of Physics and Astronomy, Proeftuinstraat 86 N3, 9000 Ghent, Belgium
[112] Konkoly Observatory, HUN-REN CSFK, MTA Centre of Excellence, Budapest, Konkoly Thege Miklós út 15-17. H-1121, Hungary
[113] MTA-CSFK Lendület Large-Scale Structure Research Group, Konkoly-Thege Miklós út 15-17, H-1121 Budapest, Hungary
[114] Université de Strasbourg, CNRS, Observatoire astronomique de Strasbourg, UMR 7550, 67000 Strasbourg, France
[115] Scuola Superiore Meridionale, Via Mezzocannone 4, 80138, Napoli, Italy
[116] Instituto de Astrofísica e Ciências do Espaço, Faculdade de Ciências, Universidade de Lisboa, Tapada da Ajuda, 1349-018 Lisboa, Portugal
[117] Institute of Cosmology and Gravitation, University of Portsmouth, Portsmouth PO1 3FX, UK
[118] Institute for Astronomy, University of Hawaii, 2680 Woodlawn Drive, Honolulu, HI 96822, USA
[119] Departamento Física Aplicada, Universidad Politécnica de Cartagena, Campus Muralla del Mar, 30202 Cartagena, Murcia, Spain
[120] Univ. Grenoble Alpes, CNRS, IPAG, 38000 Grenoble, France
[121] CEA Saclay, DFR/IRFU, Service d'Astrophysique, Bat. 709, 91191 Gif-sur-Yvette, France
[122] Department of Mathematics and Physics E. De Giorgi, University of Salento, Via per Arnesano, CP-I93, 73100, Lecce, Italy
[123] INFN, Sezione di Lecce, Via per Arnesano, CP-193, 73100, Lecce, Italy
[124] INAF-Sezione di Lecce, c/o Dipartimento Matematica e Fisica, Via per Arnesano, 73100, Lecce, Italy
[125] Dipartimento di Fisica "E. Pancini", Universita degli Studi di Napoli Federico II, Via Cinthia 6, 80126, Napoli, Italy
[126] INFN Sezione di Napoli, Universita degli Studi di Napoli "Federico II", Compl. Univ. di Monte S. Angelo, Edificio G, Via Cinthia, I-80126, Napoli, Italy
[127] Université Paris Cité, CNRS, Astroparticule et Cosmologie, 75013 Paris, France
[128] Department of Computer Science, Aalto University, PO Box 15400, Espoo, FI-00 076, Finland
[129] Ruhr University Bochum, Faculty of Physics and Astronomy, Astronomical Institute (AIRUB), German Centre for Cosmological Lensing (GCCL), 44780 Bochum, Germany
[130] DARK, Niels Bohr Institute, University of Copenhagen, Jagtvej 155, 2200 Copenhagen, Denmark
[131] Van Swinderen Institute, University of Groningen, Nijenborgh 3, 9747 AG Groningen, The Netherlands
[132] Department of Physics and Astronomy, University of the Western Cape, Bellville, Cape Town, 7535, South Africa
[133] Department of Physics and Helsinki Institute of Physics, Gustaf Hällströmin katu 2, University of Helsinki, 00014 Helsinki, Finland
[134] INAF-Osservatorio Astrofisico di Arcetri, Largo E. Fermi 5, 50125, Firenze, Italy
[135] Centro de Astrofísica da Universidade do Porto, Rua das Estrelas, 4150-762 Porto, Portugal
[136] Dipartimento di Fisica, Università di Roma Tor Vergata, Via della Ricerca Scientifica 1, Roma, Italy
[137] INFN, Sezione di Roma 2, Via della Ricerca Scientifica 1, Roma, Italy
[138] HE Space for European Space Agency (ESA), Camino bajo del Castillo, s/n, Urbanizacion Villafranca del Castillo, Villanueva de la Cañada, 28692 Madrid, Spain
[139] Dipartimento di Fisica "G. Occhialini", Università degli Studi di Milano Bicocca, Piazza della Scienza 3, 20126 Milano, Italy
[140] School of Physical Sciences, The Open University, Milton Keynes, MK7 6AA, UK
[141] Department of Astrophysics, University of Zurich, Winterthurerstrasse 190, 8057 Zurich, Switzerland
[142] Space physics and astronomy research unit, University of Oulu, Pentti Kaiteran katu 1, FI-90014 Oulu, Finland
[143] Department of Mathematics and Physics, Roma Tre University, Via della Vasca Navale 84, 00146 Rome, Italy
[144] Theoretical astrophysics, Department of Physics and Astronomy, Uppsala University, Box 524, 751 20 Uppsala, Sweden
[145] Institute of Astronomy, University of Cambridge, Madingley Road, Cambridge CB3 0HA, UK

[146] Department of Astrophysical Sciences, Peyton Hall, Princeton University, Princeton, NJ 08544, USA
[147] Fakultät für Physik, Universität Bielefeld, Postfach 100131, 33501 Bielefeld, Germany
[148] Department of Physics, Centre for Extragalactic Astronomy, Durham University, South Road, Durham, DH1 3LE, UK
[149] Department of Physics and Astronomy, University of British Columbia, Vancouver, BC V6T 1Z1, Canada

⋆ e-mail: jerome.odier@lpsc.in2p3.fr

Appendix A: Zoom-in on the DR1 EWS masks

Examples of the DR1 EWS masks are presented here for observation Patch ID 4, in Figs. A.1, A.2, A.3, and A.4.

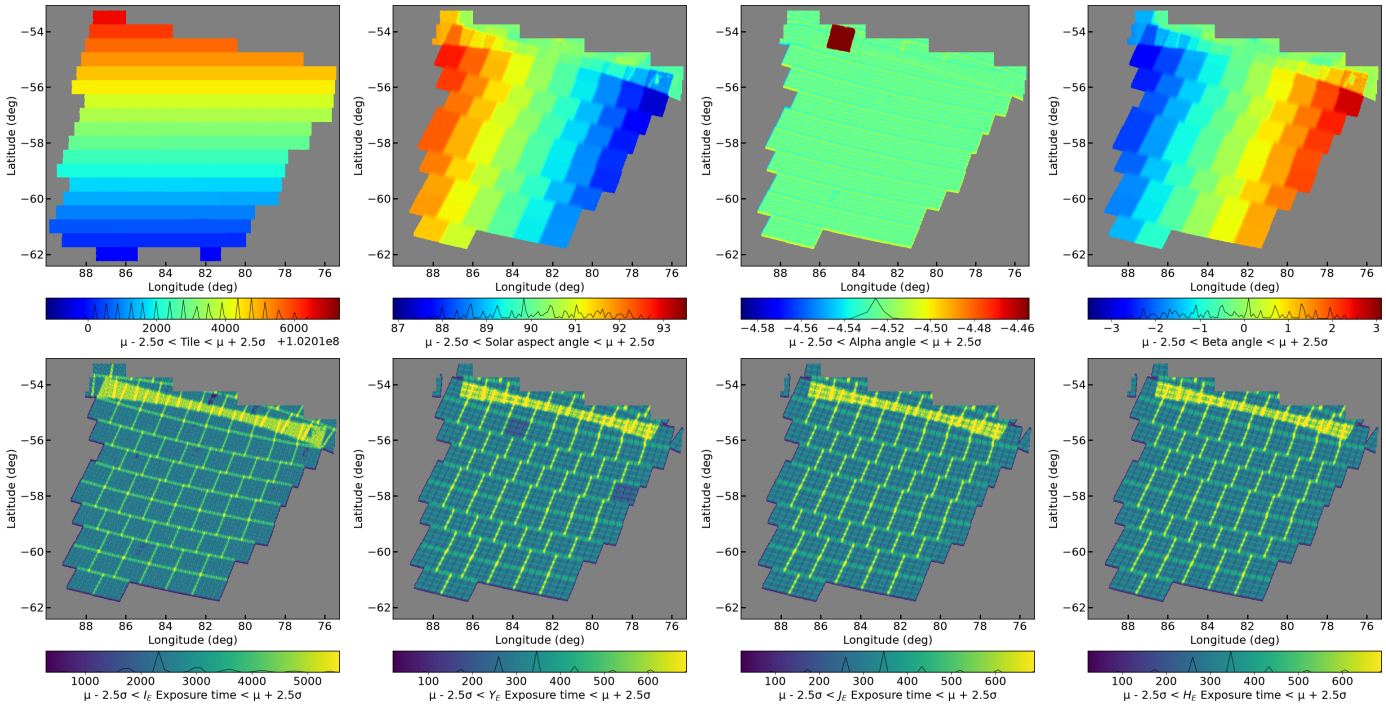


Fig. A.1. Main survey masks for the DR1 EWS Patch ID 4. From left to right, the panels show the tile index, solar aspect angle, alpha angle, and beta angle (top row), followed by the integration time for the I_E, Y_E, J_E, and H_E bands (bottom row).

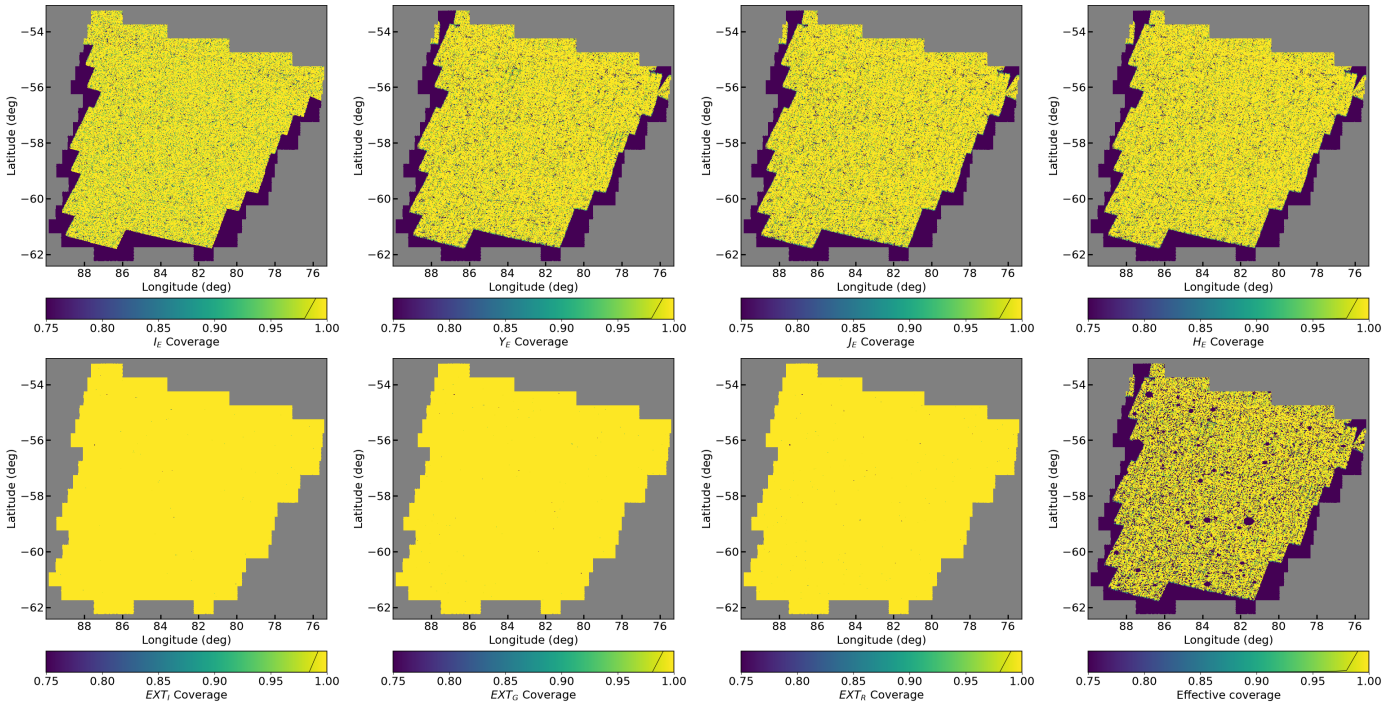


Fig. A.2. Examples of survey-definition masks for the DR1 EWS Patch ID 4. From left to right, the panels show the coverage for the I_E, Y_E, J_E, and H_E bands (top row), followed by the coverage for the available EXT bands and the combined effective coverage (bottom row). For DR1, the EXT coverage masks do not include the polygons used to mask regions affected by bright stars. This masking is currently applied only when constructing the combined effective coverage mask.

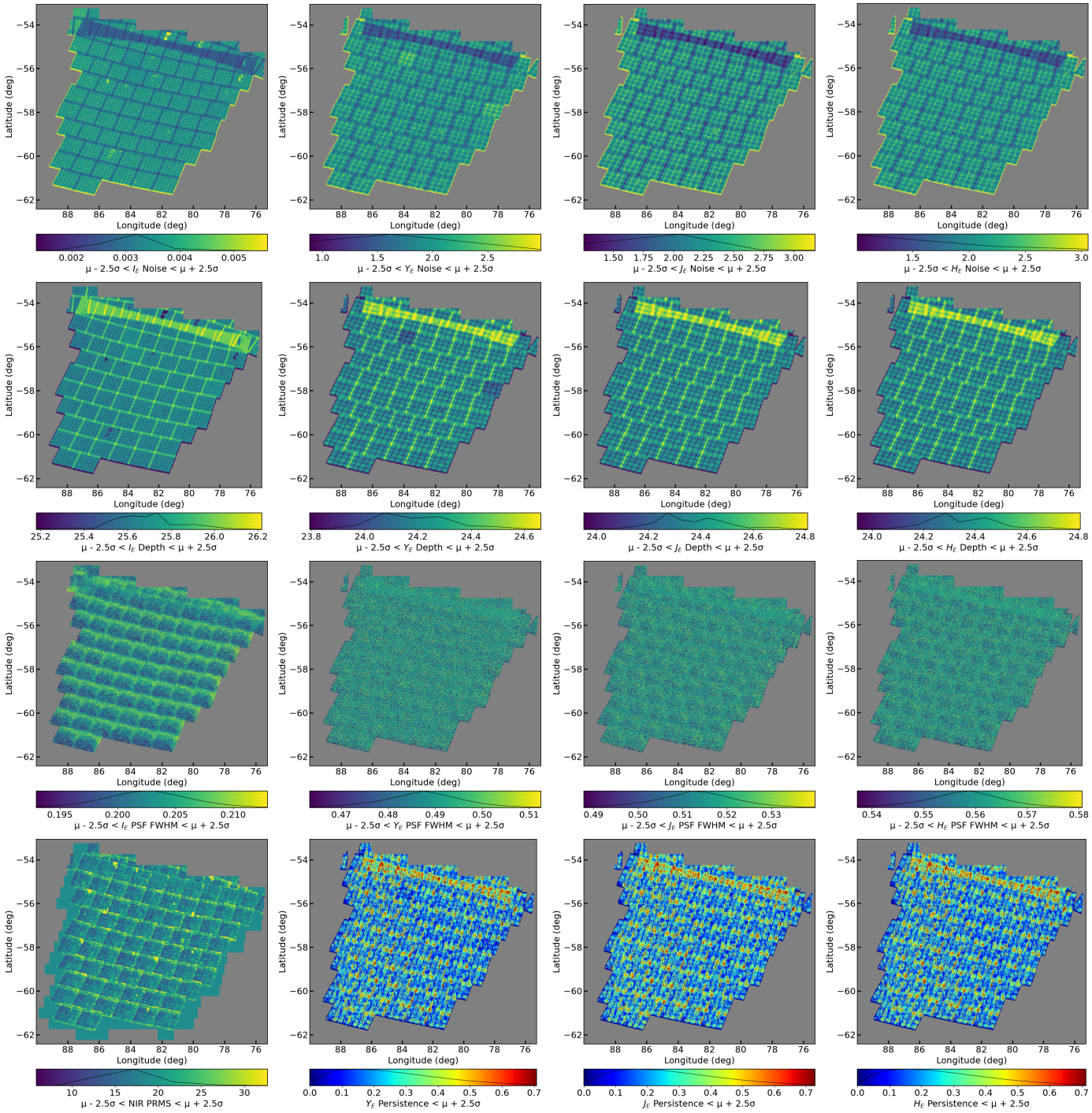


Fig. A.3. Examples of instrumental-property masks for the DR1 EWS Patch ID 4. From top to bottom, the panels show the RMS noise, depth, and PSF FWHM for the I_E, Y_E, J_E, and H_E bands, followed by the NIR PRMS and persistence masks for the NIR bands.

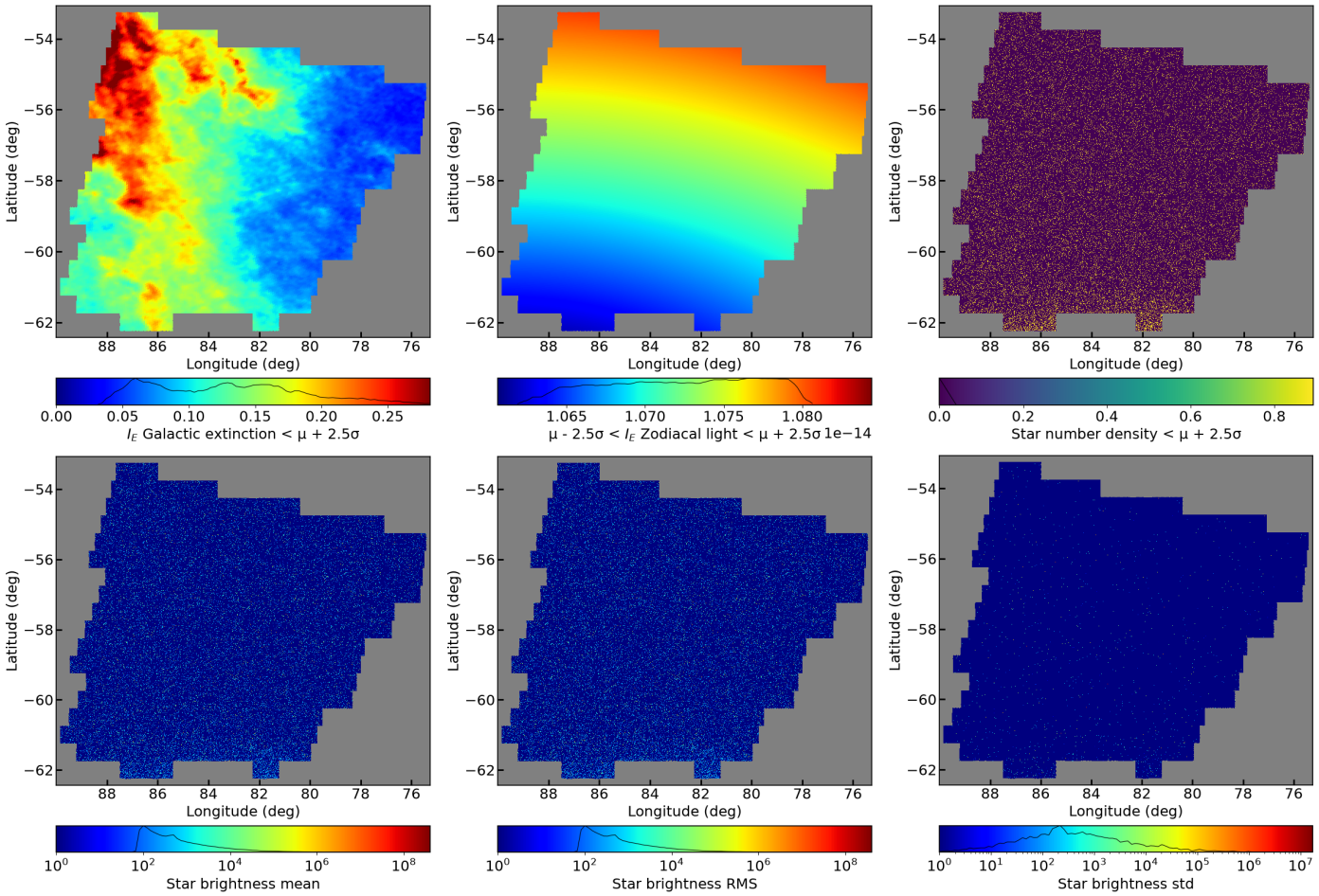


Fig. A.4. Examples of sky-emission and stellar-property masks for the DR1 EWS Patch ID 4. From left to right and from top to bottom, the panels show Galactic extinction, zodiacal light, star number density, mean star brightness, star brightness RMS, and star brightness standard deviation.

Appendix B: Photometric and instrumental properties of the Euclid Deep Fields

Tables B.1, B.2, and B.3 present statistical information for the EDFs.

Table B.1. For DR1 EDF-F, the mean, median, standard deviation (Std), percentiles (Q_{16}, Q_{25}, Q_{75}, and Q_{84}), and IQR of the distributions of integration time, RMS Noise, depth, and PSF FWHM for the four *Euclid* bands.

Band	Quantity	Mean	Median	Std	Q_{16}	Q_{25}	Q_{75}	Q_{84}	IQR
I_E	Exposures [s]	4642	4842	1070	4103	4192	5403	5492	1211
	Noise [ADU]	0.003197	0.003033	0.0008102	0.002836	0.002918	0.003204	0.003328	0.0002856
	Depth [AB mag]	25.89	25.93	0.1783	25.83	25.87	25.97	26	0.1014
	PSF FWHM [arcsec]	0.2035	0.2033	0.004154	0.1994	0.2005	0.2064	0.2077	0.005833
Y_E	Exposures [s]	582.5	610.7	134.7	523.5	523.5	698	698	174.5
	Noise [ADU]	1.74	1.675	0.3142	1.529	1.583	1.78	1.88	0.1968
	Depth [AB mag]	24.34	24.37	0.159	24.25	24.31	24.43	24.47	0.1272
	PSF FWHM [arcsec]	0.4896	0.4899	0.007884	0.4828	0.4853	0.4942	0.4965	0.008924
J_E	Exposures [s]	579.4	610.7	135.3	523.5	523.5	698	698	174.5
	Noise [ADU]	2.017	1.939	0.3633	1.768	1.835	2.072	2.178	0.2366
	Depth [AB mag]	24.48	24.51	0.1596	24.39	24.44	24.57	24.61	0.1317
	PSF FWHM [arcsec]	0.5155	0.5158	0.008394	0.5083	0.511	0.5205	0.5229	0.009538
H_E	Exposures [s]	570.3	610.7	144.1	436.2	523.5	698	698	174.5
	Noise [ADU]	1.864	1.776	0.3511	1.618	1.679	1.928	2.044	0.2489
	Depth [AB mag]	24.47	24.51	0.1694	24.35	24.42	24.57	24.61	0.1501
	PSF FWHM [arcsec]	0.5602	0.5606	0.00712	0.5543	0.5565	0.5644	0.5664	0.007904

Table B.2. As Table B.1 for DR1 EDF-N.

Band	Quantity	Mean	Median	Std	Q_{16}	Q_{25}	Q_{75}	Q_{84}	IQR
I_E	Exposures [s]	21 373	25 332	8888	8092	17 687	27 282	28 111	9595
	Noise [ADU]	0.001635	0.001221	0.001115	0.001162	0.001176	0.001454	0.002123	0.0002775
	Depth [AB mag]	26.72	26.91	0.4366	26.31	26.72	26.95	26.97	0.23
	PSF FWHM [arcsec]	0.2033	0.2032	0.002332	0.2016	0.2021	0.2043	0.2049	0.002179
Y_E	Exposures [s]	2565	2966	1048	1047	2268	3228	3315	960
	Noise [ADU]	0.92	0.7123	0.8847	0.6729	0.684	0.8261	1.202	0.1421
	Depth [AB mag]	25.12	25.3	0.402	24.73	25.14	25.34	25.36	0.205
	PSF FWHM [arcsec]	0.4918	0.4924	0.005346	0.4888	0.4902	0.4944	0.4954	0.004196
J_E	Exposures [s]	2490	2966	1006	960	2181	3141	3228	960
	Noise [ADU]	1.055	0.8213	1.07	0.7784	0.7898	0.9519	1.372	0.1621
	Depth [AB mag]	25.27	25.44	0.3952	24.89	25.28	25.49	25.5	0.2026
	PSF FWHM [arcsec]	0.5181	0.5186	0.005552	0.5149	0.5163	0.5207	0.5218	0.004441
H_E	Exposures [s]	2554	2966	1044	1047	2181	3228	3315	1047
	Noise [ADU]	0.9624	0.7467	0.8437	0.705	0.7167	0.8694	1.257	0.1528
	Depth [AB mag]	25.27	25.45	0.401	24.88	25.28	25.49	25.51	0.2098
	PSF FWHM [arcsec]	0.5631	0.5637	0.004943	0.5605	0.5618	0.5655	0.5664	0.003773

Table B.3. As Table B.1 for DR1 EDF-S.

Band	Quantity	Mean	Median	Std	Q_{16}	Q_{25}	Q_{75}	Q_{84}	IQR
I_E	Exposures [s]	20 275	23 561	7669	10 245	18 898	25 040	25 714	6142
	Noise [ADU]	0.00168	0.001296	0.001154	0.001246	0.00126	0.001451	0.001962	0.0001915
	Depth [AB mag]	26.68	26.85	0.4079	26.4	26.73	26.88	26.89	0.1537
	PSF FWHM [arcsec]	0.2035	0.2034	0.002228	0.2019	0.2024	0.2044	0.205	0.002045
Y_E	Exposures [s]	2505	2879	947	1221	2356	3141	3228	785
	Noise [ADU]	0.9221	0.7313	0.932	0.6972	0.7065	0.8173	1.099	0.1109
	Depth [AB mag]	25.11	25.27	0.3784	24.83	25.15	25.31	25.32	0.1583
	PSF FWHM [arcsec]	0.4916	0.4921	0.005175	0.4887	0.49	0.4941	0.4951	0.004157
J_E	Exposures [s]	2514	2966	953	1221	2356	3141	3228	785
	Noise [ADU]	1.048	0.8318	0.9247	0.7931	0.8035	0.9321	1.253	0.1286
	Depth [AB mag]	25.27	25.43	0.378	24.99	25.31	25.47	25.48	0.1612
	PSF FWHM [arcsec]	0.5177	0.5182	0.005378	0.5146	0.5159	0.5203	0.5214	0.004376
H_E	Exposures [s]	2511	2966	952.7	1221	2268	3141	3228	872
	Noise [ADU]	0.9673	0.7651	1.208	0.7291	0.7388	0.8596	1.155	0.1209
	Depth [AB mag]	25.26	25.42	0.3795	24.97	25.3	25.46	25.47	0.1645
	PSF FWHM [arcsec]	0.5629	0.5634	0.00469	0.5603	0.5615	0.5652	0.5661	0.003726